

Wavefront engineering to enhance atom-light interaction

Chow Chang Hoong

(B.Sc (Hons), NUS)

A thesis submitted for the degree of
Master of Science

Department of Physics

National University of Singapore

2018

Supervisor:

Professor Christian Kurtsiefer

Examiners:

Professor Valerio Scarani

Assistant Professor Li Wenhui

Declaration

I hereby declare that this thesis is my original work and it has been written by me in its entirety. I have duly acknowledged all the sources of information which have been used in the thesis.

This thesis has also not been submitted for any degree in any university previously.

Handwritten signature in Chinese characters: 周鎮鴻

Chow Chang Hoong

July 2018

Acknowledgements

First and foremost, I would like to express my greatest gratitude to my supervisor, Professor Christian Kurtsiefer for the guidance and opportunity to work on this interesting project. It has been an amazing year and wonderful experience to work in this group.

My sincere thanks to my mentors, Matthias and Wilson, who introduced me to atomic physics, electronics, scripting, and basically everything in the lab. Not to mention the continual output of ideas from you two when the two dimensional knife-edge measurement seemed to come to a dead end. Enjoy the greener pastures!

To Boon Long, Chi Huan and Janet, thank you for the support, small talks, and of course, coffee pauses after I have shifted my desk. Thanks to Brenda and Adrian for proofreading the draft. Also, big thanks to everyone else in the lab, it has been a great time working with you all.

Contents

1	Introduction	1
2	Gaussian Beam Model	5
2.1	Beam Propagation	5
2.2	Beam Focusing	6
3	Knife-edge Measurement	9
3.1	Principles	9
3.2	Experimental Setup	11
3.3	Waist Measurement	13
3.4	Varying the Aperture Utilization of the Lens	16
3.4.1	Alignment Procedures	17
3.4.2	Preliminary Results	17
4	One-dimensional Optimization	20
4.1	Spatial Light Modulator	20
4.1.1	Implementations	21
4.2	Zernike Polynomials	25
4.3	Waist Optimization	26
4.3.1	Gradient Search Algorithm	26
4.3.2	Results and Discussions	29
4.4	Intensity Optimization	37
4.4.1	Intensity Reconstruction	37
4.4.2	Experimental Setup	38
4.4.3	Results and Discussions	40

5	Two-dimensional Optimization	45
5.1	Two-dimensional Knife-edge Method	45
5.2	Validity of the Measured Area	47
5.3	Experimental Setup	49
5.4	Results and Discussions	55
6	Conclusion and Ongoing Work	60
7	Appendices	62
7.1	SLM settings	62
7.1.1	Determination of Beam Position	62
7.1.2	Characteristic Radius	63
7.2	Zernike Dimension	64

Abstract

In this thesis, we present a method of achieving a diffraction-limited focal spot size when a collimated laser beam is focused down with a high NA lens ($\text{NA} = 0.55$, $f = 4.51$ mm). We use a spatial light modulator to correct for optical aberrations due to the focusing optics. We analyze the transverse beam profile at the focus of the high NA lens using the knife-edge method. The beam waist radius, peak intensity, and beam cross-sectional area are taken as the figure of merit for an optimization algorithm to improve focusing. In this thesis, we report on the setting up of lenses and a razor blade mounted onto a piezo-driven stage to perform the automated knife-edge measurement. An optimization algorithm based on Zernike polynomials that we developed manages to reduce the waist radius. Reconstruction of the Gaussian beam intensity profile at the focus after optimization shows an increase in the peak of the light intensity. For the largest input beam used in our experiment ($w_{in} = 1.96$ mm), the two dimensional area optimization algorithm yields a peak intensity improvement of 17.6% (x -axis) and 16.3% (y -axis) compared to the uncorrected beam.

1 Introduction

In the past two decades, research in the field of quantum information has seen tremendous growth [1, 2]. By making use of properties such as superposition and entanglement, algorithms can greatly reduce computational complexity and outperform their classical counterparts, some examples of which include Shor's algorithm for the factorization of large numbers [3] and Grover's algorithm for database searching [4]. For these quantum algorithms to be practically useful, quantum computing platforms need to scale up [5].

One feasible design is to construct a distributed quantum network consisting of stationary nodes, formed by quantum emitters which process and store information, and flying qubits, formed by photons which play the role as the carriers of information [6]. Numerous physical systems have been suggested as candidates for the implementation of a large scale quantum network, such as Rydberg atoms [7, 8], trapped ions [9, 10], nitrogen-vacancy centres [11], quantum dots [12] and trapped atoms [13, 14]. Here we will focus on single trapped neutral atoms.

One of the major stumbling blocks of this system lies in achieving efficient transfer of quantum information from a photonic qubit to an atomic qubit. One common method of enhancing the atom-light interaction is to place atoms in a high-finesse cavity [15]. An alternative approach is to couple a single trapped atom to the light field focused by a large numerical aperture (NA) lens [16]. Motivated by the fact that the absorption cross-sectional area of an atom is on the order of the square of the resonant transition wavelength, which is smaller than the possible attainable diffraction-limited spot size of a focused beam, efforts are devoted to maximize the overlap of incident light and the radiation emission mode of a single atom [17]. Theoretically, it has been shown that it is possible to reach a near-deterministic absorption of single photons for dedicated focusing geometries, for

example by using a parabolic mirror as a mode converter [18].

We could characterize the interaction strength between single atoms and light based on the extinction of a probe laser. The total transmitted electric field is a superposition of the collected probe field and the field scattered by the atom. The phase difference between these two fields will result in destructive interference, which leads to an extinction of the transmitted beam. For a numerical aperture of one (focusing from half solid angle) and an incoming field in the dipole radiation mode, complete extinction in the forward direction is predicted [19]. Some of the important milestones of extinction measurements are recorded in Table 1. The first transmission spectrum of a single atom was observed for a $^{198}\text{Hg}^+$ ion. The absorption probability of the probe photons in that experiment was estimated to be around 2.5×10^{-5} [20]. Recent experiments on single molecules and semiconductor quantum dots reported an extinction up to 22% [21, 22]. In our lab, the maximum extinction experimentally achieved in a setup in which the focusing optics covered most of the solid angle (adapting a 4π microscopy technique with lenses of $\text{NA} = 0.75$) demonstrated an extinction of around 36.6%, which is a factor of 2 from the theoretical limit of 75% [23]. Similarly, exceptionally high coupling efficiency of a trapped $^{174}\text{Yb}^+$ ion is reported when illuminated with laser focused with parabolic mirrors from a nearly full solid angle [24, 25].

Although substantial attenuation of the forward travelling beam has been reported, the interaction strengths observed with these configurations still fall short of their theoretical limits. It has been hypothesized that the residual temperature of the cooled single atom could be a limiting factor for atom-light interaction. For our setup described in [23], extrapolation from experimental results has shown that only a moderate improvement of interaction strength is expected by cooling to the motional ground state of atom [28]. Here we focus on the second pos-

Table 1: State of the art of atom-light coupling in free space. For experiments where only the extinction ϵ is reported, the coupling efficiency Λ , which describes the spatial mode overlap between the input probe mode and the atomic dipole mode, is calculated with $\epsilon = 4\Lambda(1 - \Lambda)$ [26].

Experimental system	Year	Extinction ϵ	Coupling efficiency Λ
Trapped ion [20]	1987	$\leq 0.1\%$	$\leq 0.025\%$
Quantum dot [22]	2007	12%	3.1%
Molecule in matrix [21]	2008	22%	5.8%
Trapped atom (lens NA = 0.55) [27]	2008	10%	2.6%
Trapped ion (parabolic mirror) [24]	2014	27%	7.2%
Trapped atom (lens NA = 0.75) [23]	2017	36.6%	10.2%
Trapped ion (parabolic mirror) [25]	2017	47.3%	13.7%

sible experimental limitation due to the imperfections (non-ideal behaviours) of the focusing optics which cause distorted spherical wavefronts, leading to weak atom-light interaction.

In this thesis we are correcting the aberrations due to non-ideal optical elements by using a spatial light modulator (SLM) to achieve a diffraction-limited focal spot size. The general strategy is to analyze the field intensity distribution at the focus of a high NA lens and to apply aberration corrections to the incoming beam. As the first step, we study the transverse beam profile of a focusing beam in free space without a single atom.

- Method to characterize the beam waist: We started the experiment by characterizing the beam with one-dimensional knife-edge measurement, and this serves as the starting point for this thesis. We later have present a two-dimensional knife-edge technique to obtain transverse beam waist radii along two orthogonal directions.
- Method to reduce the beam waist: A scheme for correcting the aberrations based on beam waist measurement is applied using a SLM. An optimization algorithm is employed to obtain a spatial phase pattern that can minimize

the beam waist radius at the focus. The beam profile at the end of optimization is carefully studied.

Thesis Outline

This thesis is organized as follows. Section 2 reviews the paraxial Gaussian model used to describe a laser beam profile. In Section 3, we present the knife-edge technique to characterize the beam waist. In particular, we study the waist radius and M^2 factor that we obtained at the focus for different incident beam waists. In Section 4, we measure the beam waist along one transverse direction and discuss how wavefront aberrations can be corrected via the introduction of a SLM. To verify that reduced beam waist radius corresponds to improved focusing, we also describe another optimization scheme based on reconstructed intensity. In Section 5, we present the two-dimensional knife-edge measurement to better characterize the focal spot of laser beam. Finally, Section 6 summarizes the thesis and suggests avenues for future investigation.

2 Gaussian Beam Model

This section presents the Gaussian beam model for describing beam intensity profiles used in our experiment. The passage of a Gaussian beam through a perfect lens and the assumptions made are also discussed [29].

2.1 Beam Propagation

Consider a linearly polarized, monochromatic, and cylindrically symmetric Gaussian laser beam with electric field amplitude described by

$$\vec{E}(r, z) = \vec{E}_0 \frac{w_0}{w(z)} \exp\left(-\frac{r^2}{w(z)^2}\right) \exp\left(-i\left(kz + k\frac{r^2}{2R(z)}\right)\right), \quad (1)$$

where r and z are the radial and axial directions of the beam in cylindrical coordinates; k the wave number; $w(z)$ the beam radius at position z , defined as the radius at which the electric field amplitude drops to $1/e$ of its axial value; w_0 the waist radius at the focus and $R(z)$ is the radius of curvature of the wavefront of the beam at position z .

One important question is how rapidly an ideal Gaussian beam expands as it propagates away from the waist region. The variation of beam radius $w(z)$ along the propagation direction is given by

$$w(z) = w_0 \sqrt{1 + \left(\frac{z - z_0}{z_R}\right)^2}, \quad (2)$$

where $z_R = \frac{\pi w_0^2}{\lambda}$ is the Rayleigh length, λ denotes the wavelength of laser beam, and z_0 is the location of the focus. The evolution of radius of curvature $R(z)$ is given by

$$R(z) = (z - z_0) \left[1 + \left(\frac{z_R}{z - z_0}\right)^2 \right]. \quad (3)$$

From Eq. 1, one can see that the geometric dependence of a Gaussian beam's electric field is governed by $w(z)$ and $R(z)$, which are both functions of position $(z - z_0)$ and Rayleigh length z_R .

One has to take note that real laser beams are not ideal Gaussian beams. To account for the beam divergence due to non-Gaussian modes, we introduce the beam quality factor M^2 [30]. One modifies the waist evolution (Eq. 2) to

$$w(z) = w_0 \sqrt{1 + \left(\frac{z - z_0}{z_R} M^2\right)^2} . \quad (4)$$

The M^2 term here is defined as the ratio of measured to ideal beam divergence. For a perfect Gaussian beam, $M^2 = 1$. Physical beams generally have $M^2 > 1$.

2.2 Beam Focusing

For the purpose of our study, we suppose that the Gaussian beam traverses a perfect lens with focal length f , i.e., we assume that the lens is aberration free and not affected by the aperture size. In this experiment, we work with low to moderate focusing (focusing parameter u , defined in Eq. 11, is smaller than 0.5). Therefore, when the propagation direction of light deviates slightly from the optical axis, the light path can be approximated with the lowest order terms of divergence angle. This is referred to as the paraxial approximation, which is valid when the incident beam size is much smaller than the focal length f . The validity of the paraxial approximation is further discussed in Section 3.4. Under the paraxial approximation, the change in electric field after passing through a lens is denoted by

$$\vec{E}' = e^{ikr^2/2f} \vec{E} , \quad (5)$$

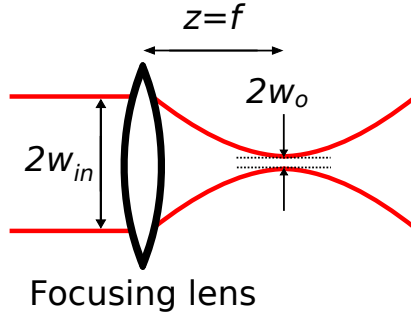


Figure 1: Focusing of a Gaussian beam by an ideal lens. w_{in} : waist radius right before the lens. w_0 : waist radius at the focal point. The two radii are related by Eq. 6.

where \vec{E}' is the electric field immediately after a lens. Here we use prime to represent beam properties in the image space. One important feature of \vec{E}' is that it remains Gaussian, with $w' = w$ and $\frac{1}{R'} = \frac{1}{R} - \frac{1}{f}$ where w and R (w' and R') are the beam radius and the radius of curvature right before the lens (after the lens).

The beam radius is at its minimum near the focus. By manipulating Eq. 2 we are able to relate the beam radius at the lens w_{in} and beam radius at the focus w_0 :

$$w_{in} = w_0 \sqrt{1 + \left(\frac{f\lambda}{\pi w_0^2}\right)^2}.$$

Near the focus, w_0 and λ are on the same order while $f \gg w_0$. The expression above can be further simplified, which gives

$$w_{in} \simeq \frac{f\lambda}{\pi w_0}. \quad (6)$$

where w_{in} is the beam radius before the lens and f is the focal length.

Aperture Effects

All real optical systems have finite apertures. When a laser beam is truncated by an aperture, the beam profile at the focal point is no longer a Gaussian, but a convolution of an Airy pattern and Gaussian. The aperture effect is more severe if the beam radius is close to the aperture size. We can characterize this effect by the fraction of power blocked by the aperture (clipping κ), defined as

$$\begin{aligned}\kappa &= \frac{\int_{R_{CA}}^{\infty} |\vec{E}(r)|^2 2\pi r dr}{\int_0^{\infty} |\vec{E}(r)|^2 2\pi r dr} \\ &= e^{-2R_{CA}^2/w_{in}^2},\end{aligned}\tag{7}$$

where R_{CA} is the clear aperture (CA) radius of the main focusing lens. For beam sizes in this experiment, κ due to finite aperture of lens is low (less than 3.5%). κ in our experiment is further discussed in Section 3.4.

Validity of the Scalar Wave Approximation

For a large numerical aperture lens, one has to take polarization into account. In fact, the electric field was treated as a scalar field in previous discussions. In the example of a beam which is initially linearly polarized, immediately after the lens, the polarization for each ray has a different radial polarization component. As the electric field with different polarizations does not simply add up, a vectorial focusing theory is required. Studies have shown that the transverse beam profile is elongated in the polarization direction [31]. We measure the beam waist in the same direction as the polarization vector in the experiment as to not underestimate the beam size.

3 Knife-edge Measurement

This section describes the scanning knife-edge technique that is used to experimentally measure the beam waist radius. The experimental arrangement is also shown. We vary the input beam waist radii and determine the resulting beam waist radii at the focus of an aspheric lens.

3.1 Principles

The simplest method to characterize the transverse beam profile of a laser beam would be to use a camera, and evaluate the light intensity at each individual pixel. However, typical camera pixels have dimensions of about a few micrometers and hence, this technique cannot be applied for focal spots that are less than a micrometer. Applicable methods include the knife-edge, point scan, convolution scan, and slit method. Both the point and convolution scan require fluorescence labeled latex beads and fluorescent sheets [32] which are not adaptable to an automated waist optimization experiment. For the slit method, the beam is probed with a small slit of width Δ . The Gaussian profile is constructed from the amount of light transmitted through the small slit. This method requires the slit width to be roughly 20 times smaller than the waist radius [33], which is experimentally unachievable ($\Delta \simeq 40$ nm). Here, we have decided to use the knife-edge scanning technique, which is a well known method that is capable of performing submicron waist measurements [34].

The operation principle of this method is based on an opaque knife pad or razor blade which is line-scanned through the transverse cross-section of the beam under study. While the blade moves transversely to block the beam in one axis, the power of the transmitted light beam is continuously recorded by a photodetector.

The transmitted power when the razor blade moves along the x -axis is given by the integration of the Gaussian electric field amplitude given in Eq. 1:

$$\begin{aligned} P_z(x) &= \frac{\epsilon_0}{2} \int_{-\infty}^x \int_{-\infty}^{\infty} |\vec{E}|^2 dx' dy' \\ &= P_0 \left\{ \frac{1}{2} + \frac{1}{2} \operatorname{erf} \left[\frac{\sqrt{2}(x - x_0)}{w(z)} \right] \right\}, \end{aligned} \quad (8)$$

where P_0 is the total power of laser beam. The beam profile can be tomographically reconstructed from knife-edge measurement performed in different transverse directions.

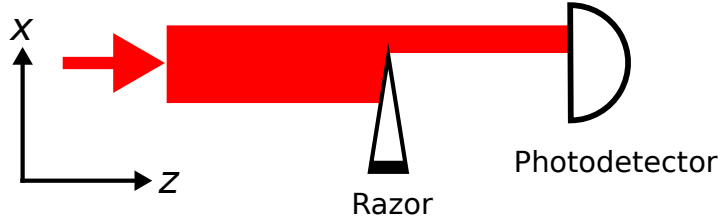


Figure 2: Simplified scheme for the measurement of laser beam radius using the knife-edge technique.

Experimentally, even if the razor blade completely blocks the beam, the photodiode still measures a small background signal. Hence, we modify the previous equation (Eq. 8) to

$$P_z(x) = P_0 \left\{ \frac{1}{2} + \frac{1}{2} \operatorname{erf} \left[\frac{\sqrt{2}(x - x_0)}{w(z)} \right] \right\} + C_p, \quad (9)$$

where C_p is a constant that can be determined when the beam is completely blocked which accounts for the background light.

3.2 Experimental Setup

The schematic diagram of our optical setup is shown in Figure 3. The heart of our setup consists of two identical aspheric lenses of $\text{NA} = 0.55$, $f = 4.51$ mm (Thorlabs C230 TMD-B) mounted in a confocal arrangement. A laser beam is delivered from a single mode fiber and collimated with a triplet fiber optic coupler (Thorlabs TC18FC-780) which outputs a beam with waist radius of 1.96 mm. A telescope in confocal arrangement is placed before the aspheric lenses to manipulate the input beam radius. The linearly polarized Gaussian laser beam focused by the first lens (test lens) is then recollimated by the second lens (collimating lens). We choose to work with a laser wavelength of 780 nm because this wavelength drives the cycling transition between $5^2\text{S}_{1/2}$ and $5^2\text{P}_{3/2}$ of ^{87}Rb that is used for the cooling and trapping of Rubidium atoms. A sharp razor blade (Gillette 7 o'clock Super Stainless Razor Blade), mounted onto a piezo-driven motorized translation stage (P-611.3S NanoCube PI XYZ Piezo Stage) driven by E-625 Piezo Servo Controller, is placed near the focus of the test lens to block the beam partially. Our piezo system has a travel range of $100\ \mu\text{m}$ with a typical resolution of 1 nm. For each axis, the translation stage is integrated with a micrometer that allows the coarse positioning of the blade with a resolution of $5\ \mu\text{m}$. The blade moves transversely in the focal plane (x -direction) to cut the beam, and along the beam propagation direction (z -direction) to access the waist region. The transmitted light after the collimating lens is detected using a silicon p-i-n photodiode (Hamamatsu S5107).

Initially, the beam waist radius measured using the knife-edge method was always two to three times larger than the theoretical prediction for an ideal Gaussian beam. The beam quality factor M^2 measured was consistently smaller than 1, approximately 0.7 which was found due to a wrong calibration of the piezo trans-

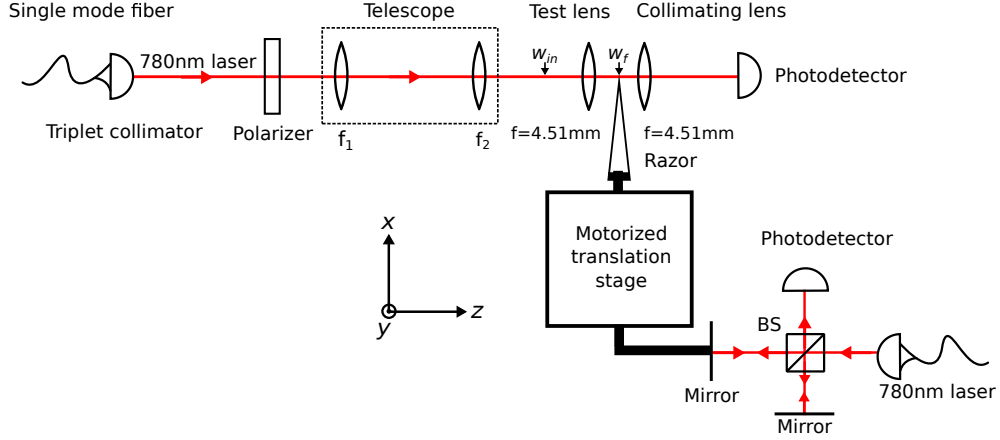


Figure 3: Schematic depiction of the knife-edge measurement with a demagnifying telescope. A photodetector measures the transmitted beam cut by a razor blade. The position of the blade is calibrated using a Michelson interferometer. The magnification of the telescope determines the incident beam waist. BS: Beamsplitter.

lation stage. The blade was translated at step sizes of $0.23 \mu\text{m}$ instead of $0.25 \mu\text{m}$. Hence, we calibrated the position of razor blade via a Michelson interferometer. Along with the razor blade, a mirror is attached to the translation stage. The mirror plays the role as a reflector for one of the interferometer arms which provides an accurate position calibration of the blade in the direction perpendicular to the beam, as shown in Figure 3.

The photodetector power reading recorded as the razor is being translated across the beam is fit to

$$V(\tilde{x}) = A + B \cos\left(\frac{2\pi}{\lambda} 2\alpha\tilde{x} + \phi\right), \quad (10)$$

where \tilde{x} is the input position. A , B , α and ϕ are all fitting parameters. α is the calibration factor that gives the real position $\alpha\tilde{x}$ (see Figure 4). The same calibration is also conducted along y and z directions.

We determine the calibration factors for the three piezo axes and construct a

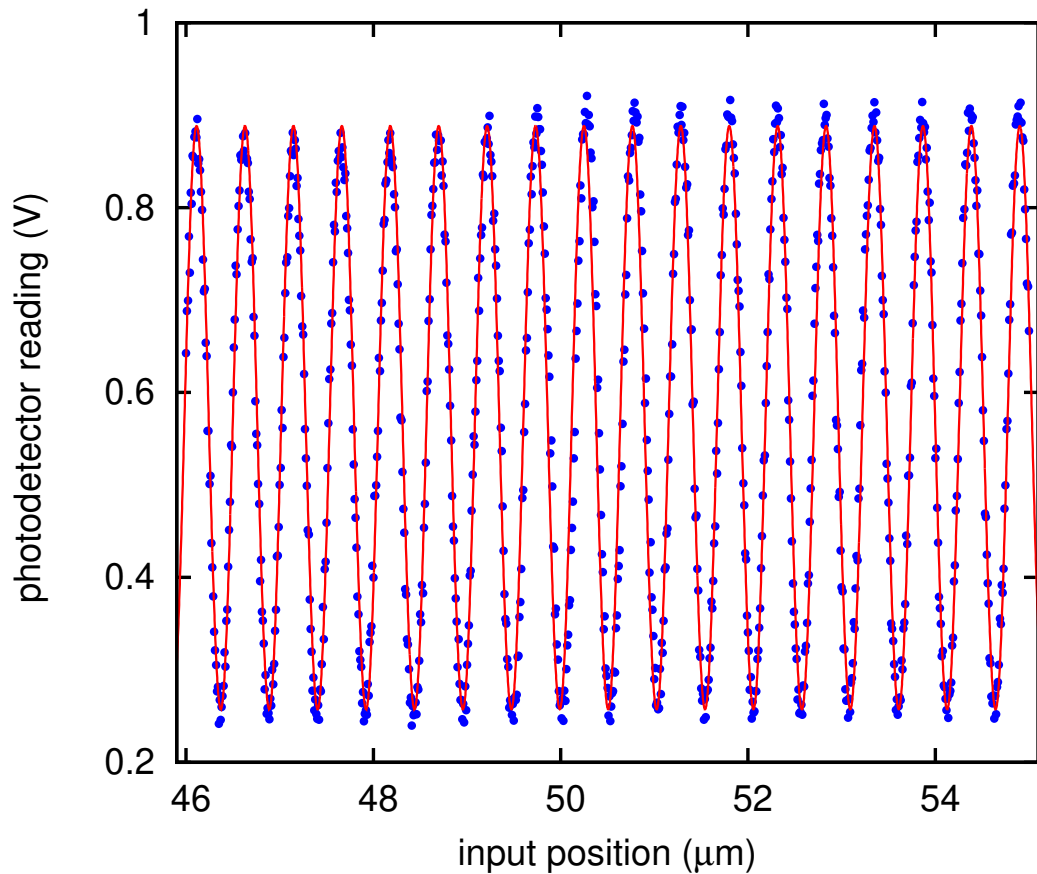


Figure 4: Typical interferometer fringes data for a single knife-edge cut along x -direction. The best fit gives $\alpha = 0.754 \pm 0.003$. Blue dots: data measured by a photodetector, red line: fit to Eq. 10.

lookup table that converts input voltages to their correct positions.

3.3 Waist Measurement

To extract the beam waist parameter with the knife-edge method, the change in transmitted power of the laser beam is measured as the razor is being translated across the beam. The razor is scanned across a $10.6\text{-}\mu\text{m}$ range at intervals of 75 nm along x -direction. The beam radius is then determined by fitting the data with the transmitted power error function (Eq. 9). An example is illustrated in Figure 5. Approximately 30 of these x -directional cuts are recorded at intervals

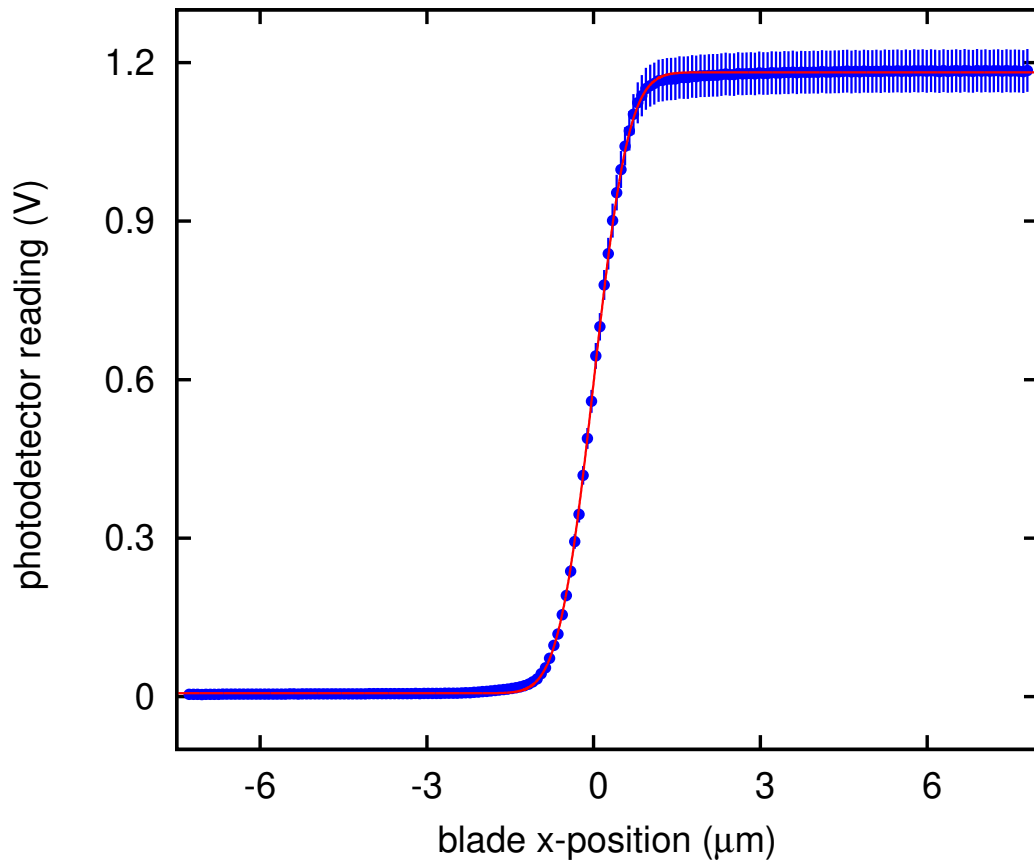


Figure 5: Typical transmitted power measured by the photodetector for a single knife-edge cut along x -direction. The fit to Eqn. 9 gives $w = 0.999 \pm 0.005 \mu\text{m}$. Error bars represent the ambient light noise and laser intensity noise (taken to be 2% of transmitted power).

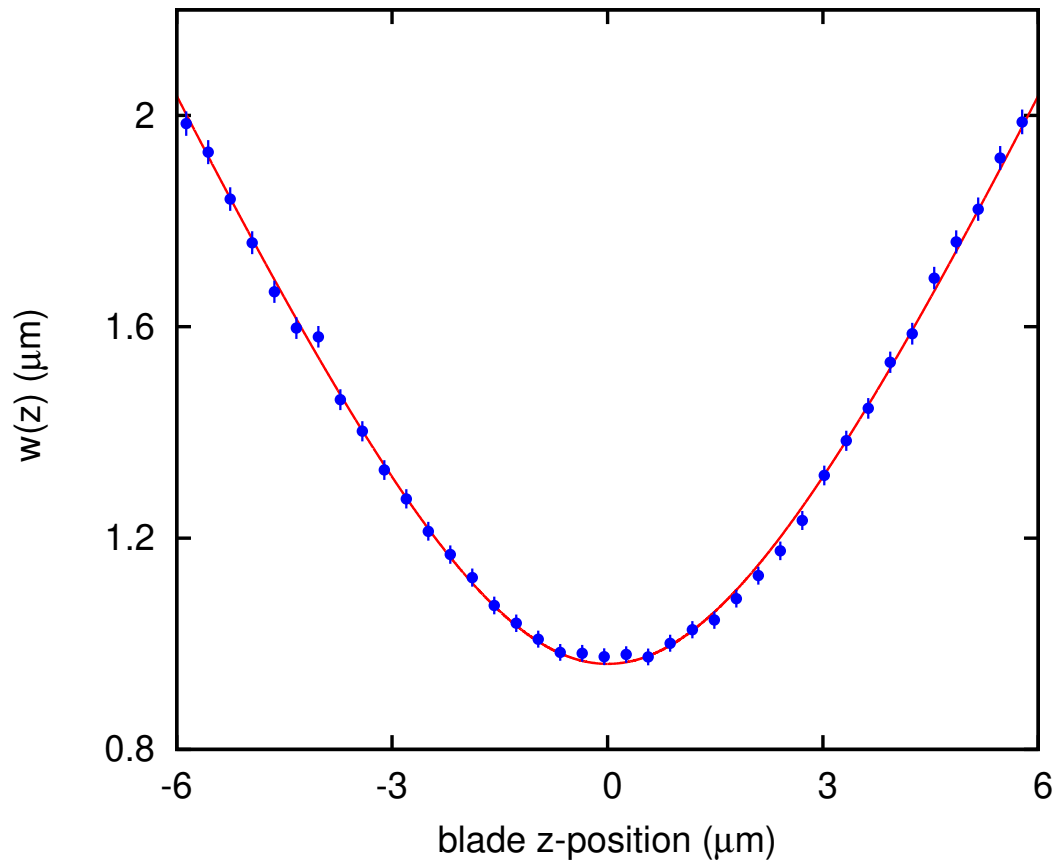


Figure 6: Beam radius near focal point, the best fit gives the waist radius and M^2 , which are determined to be $w_0 = 0.962 \pm 0.003 \mu\text{m}$ and $M^2 = 1.160 \pm 0.004$. Blue dots: fitted waist along x -direction (Eq. 9), red line: fit to waist evolution (Eq. 4). Error bars represent one standard deviation of propagated fitting uncertainties.

of $0.23\ \mu\text{m}$ along the beam propagation direction centered around the focal point. To obtain the minimum beam waist, the waist measurements from each of these cuts are fit to Eq. 4. One of such fit is shown in Figure 6.

3.4 Varying the Aperture Utilization of the Lens

We expect that lens errors would be more severe for beams that utilize a larger portion of the clear aperture because the rays passing through the edge of the lens could be focused down to a different focal position compared to the rays passing through the center. Nevertheless, to get stronger focused light fields, the beam diameter of the collimated laser beam reaching the lens needs to be larger. To describe the strength of focused light fields, we introduce the focusing parameter u [27], defined as

$$u = \frac{w_{in}}{f} . \quad (11)$$

For this experiment, we have chosen different input waists while keeping the focal length of test lens $f = 4.51\ \text{mm}$ fixed. To arrive at different input laser beam radii of the collimated beam, a telescope consisting of two planoconvex lenses with focal lengths f_1 and f_2 needs to be set up. The four settings that were used in the experiment are summarized in Table 2.

Table 2: Summary of initial settings (calculated) for varying the input beam waist.

Telescope setting		Magnification	w_{in} (mm)	u	w_f (μm)	clipping κ (%)
f_1 (mm)	f_2 (mm)					
100	50	0.5	0.98	0.217	1.14	10^{-4}
125	75	0.6	1.18	0.261	0.95	0.01
100	75	0.75	1.47	0.326	0.76	0.26
100	100	1.0	1.96	0.435	0.57	3.5

3.4.1 Alignment Procedures

To obtain a flat wavefront for the incident beam right before the aspheric lenses, we autocollimate the beam [35], as shown in Figure 7: one lens of the telescope is attached on a translation stage that moves along the beam propagation direction. A mirror is placed right before the aspheric lenses in order to back-couple the beam into single mode fiber. The amount of light being back-coupled into the fiber is measured with a photodetector (Photodetector 1) and the telescope length L is adjusted such that the confocal arrangement maximizes the back-coupling. During the autocollimation procedure, we observe two telescope lengths L that maximize the back-coupling: one corresponds to the desired confocal arrangement $L = f_1 + f_2$, the other one focuses the laser beam at the position of Mirror 3. The two cases can be differentiated by observing the laser spot size near Mirror 3 and we always choose to work in the confocal arrangement.

After the autocollimation, the tip and tilt of the two mirrors placed before the aspheric lenses (Mirror 1 and Mirror 2) are also tuned to minimize the beam quality factor M^2 as well as to ensure that the reduced chi squared of the fit to error function is close to one.

3.4.2 Preliminary Results

The measured waist radius and the beam quality factor M^2 for four focusing parameters (different input waist radii) using the knife-edge method is shown in Figure 8. In general, the measured waist radii are larger than those predicted using the paraxial Gaussian model, especially for a larger focusing parameter u (Eqn. 11). We also see that the beam quality factor M^2 becomes larger as the focusing parameter u increases. To confirm that the larger than expected waist radii are not due to the breakdown of paraxial approximation, we also compare

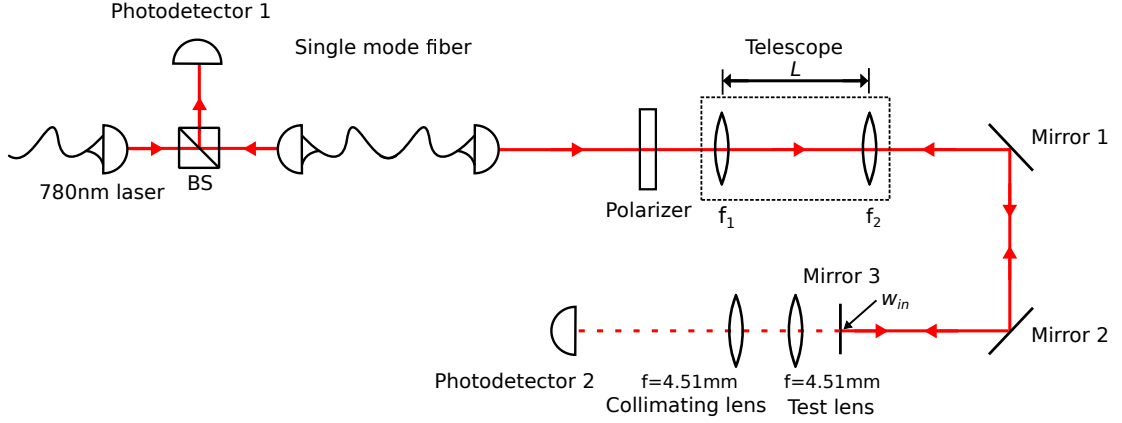


Figure 7: Schematic depiction of the autocollimation procedures to obtain flat wavefront for the incident beam illuminating the aspheric lenses. Telescope lens with focal length f_1 is attached on a translation stage to vary telescope length L in order to maximize back-coupling measured with Photodetector 1. Laser beam along dashed path is blocked by Mirror 3 that is placed right before the aspheric lenses during autocollimation. BS: Beamsplitter.

our measurements with the predictions given by the model described in [17]. We observe that the waist radius predicted under paraxial approximation is roughly 10% smaller than the prediction of the full model. However, the measured waist radii are still large compared to the prediction of the full model, particularly for a larger focusing parameter u .

There are a few possible reasons for this behaviour. First, as the input waist gets larger, it becomes more comparable with the clear aperture of the test lens ($2R_{CA} = 5.07$ mm). From Table 2 we see that there is a significant clipping κ (0.26% to 3.5%) when the focusing parameter u is greater than 0.3; hence, we expect the beam to be less Gaussian for larger focusing parameters due to diffraction at the lens edges. Besides, the beam can also be distorted by aberrations present in the optical system. The setup contains many elements, none of which are perfect. These deformations of optical elements cause aberrations in the beam. It is of our interest to study if the waist radius at the focus of the aspheric lens can be further reduced if the aberrations are corrected.

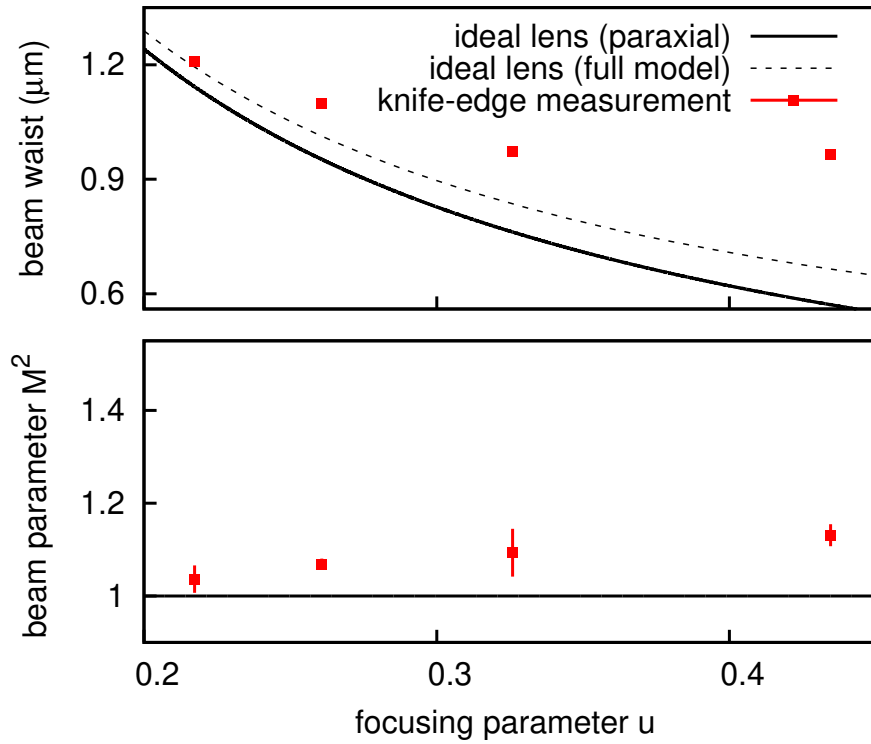


Figure 8: Waist radius and M^2 as a function of focusing parameter u . Red dots: data measured with the knife-edge technique. Black solid line: theoretical results for a paraxial ideal Gaussian beam. Black dashed line: theoretical results for the full model described in [17]. Error bars represent standard deviation of 10 repeated measurements. Error bars in top panel are smaller than symbol size.

4 One-dimensional Optimization

This section describes the minimization of focal beam spot size by correcting optical aberrations using a spatial light modulator (SLM). To this end, we vary the spatial phase pattern on the SLM to alter the wavefront of the collimated beam before the main focusing element. As the first step, we characterize the focal beam spot size based on knife-edge measurement of the beam radius in one transverse direction as described in the previous section. We optimize the focusing based on the minimization of the beam radius at the focus by varying the phase pattern supplied to the SLM using iterative gradient descent. We then compare the results of two optimization strategies; one based on the minimization of beam radius, the other one based on the maximization of peak intensity at the focus.

4.1 Spatial Light Modulator

Spatial light modulators (SLMs) are liquid crystal devices that allow dynamic manipulation of the spatial phase of the light field. A SLM is fabricated with nematic liquid crystals, aligned in a homogeneous configuration. Nematic liquid crystal molecules tend to align together in one general direction. Due to the elongated structure and orientation, the liquid crystals act together as an anisotropic dielectric. More precisely, the long axis of the molecules determines the slow axis of liquid crystals, which is responsible for the birefringence of the liquid crystal molecules.

For our SLM, when there is no applied electric field, the slow-axis of the liquid crystal molecules is aligned with the horizontal axis of the SLM. Horizontally polarized light incident on the SLM experiences the refractive index of the extraordinary axis. As the voltage applied to the liquid crystals increases, the torque on

the molecules increases, causing the molecules to align with the electric field. The alignment of the liquid crystal molecules in turn controls the phase shift of each pixel. Therefore, to modify the phase, the polarization of the input beam must be linear and horizontal relative to the axes of SLM.

4.1.1 Implementations

In our experiment, we use a LCD-based reflection SLM (Meadowlark Optics, XY P512L series). On the SLM, there are $512 \times 512 = 262144$ active pixels over an $12.8 \times 12.8 \text{ mm}^2$ array. The pixel pitch size is $25 \times 25 \mu\text{m}^2$. Each pixel can be independently controlled to modify the phase up to 2π with 16 bits of voltage resolution.

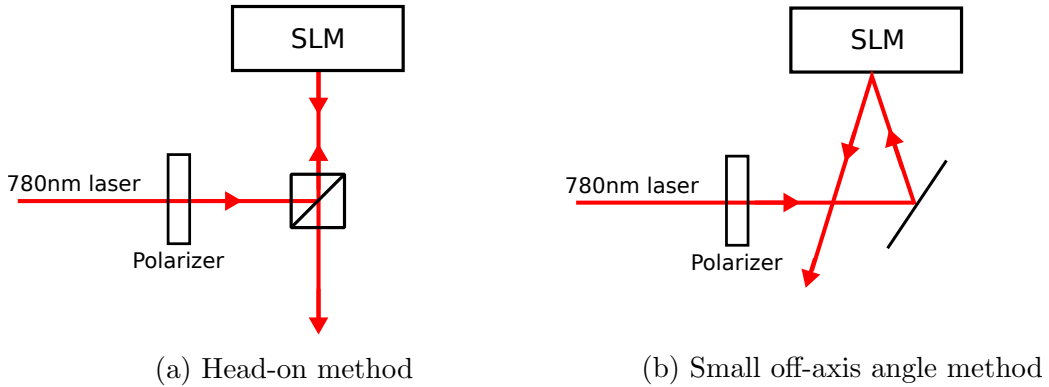


Figure 9: Optical setup to incorporate a SLM.

There are two common ways to incorporate a SLM into an optical setup. One method is to send light head-on to the SLM with a beamsplitter in order to reduce crosstalk effects due to the beam impinging on the SLM at an angle, thus illuminating more than one pixel region. In the case of a 50/50 beamsplitter, half of the light sent to the beamsplitter illuminates the SLM. The modulated light is then divided into two beams by the beamsplitter again and hence, we collect only one-fourth of total light power. The other method separates in- and outgoing

beam in an off-axis configuration. In this configuration, a laser beam is directed onto the SLM at a small off-axis angle, such that most of the modulated light can be collected. For our SLM, the thickness of the LCD layer is about $2.5 \mu\text{m}$. We keep the off-axis angle to be smaller than 11° , which corresponds to a $0.57 \mu\text{m}$ displacement in the liquid crystals, to minimize inter-pixel crosstalk. A schematic outline of our experiment with the SLM is shown in Figure 10. One has to keep in mind that the SLM can only modulate the phase of light that is linearly polarized along the horizontal axis defined by the SLM. Therefore, we use a polarizer to ensure the correct polarization of light incident on the SLM.

To modulate the spatial phase accurately, each SLM device is shipped with two customized documents:

1. Lookup table for linearization: Each of the SLM pixels can be set with $2^{16} = 65536$ discrete voltage states. The response of the liquid crystal molecules to the applied voltage is not linear. To account for this, an additional step needs to be included to convert input pixel values to voltage states that yield linear output phase response. For our SLM, the conversion is illustrated in Figure 11.
2. Surface correction phase mask: Due to the manufacturing process, the SLM screen surface is not flat; it is slightly curved with a peak-to-valley deviation of 1.28λ at $\lambda = 780 \text{ nm}$. The non-flatness results in wavefront distortion of the laser beam, even when a spatially uniform phase mask is uploaded to the SLM. The manufacturer provides us a surface correction phase mask that can compensate for this offset. With the surface correction phase mask, the SLM functions like a flat mirror. This surface correction phase mask is always added to the phase patterns that we display on the SLM.

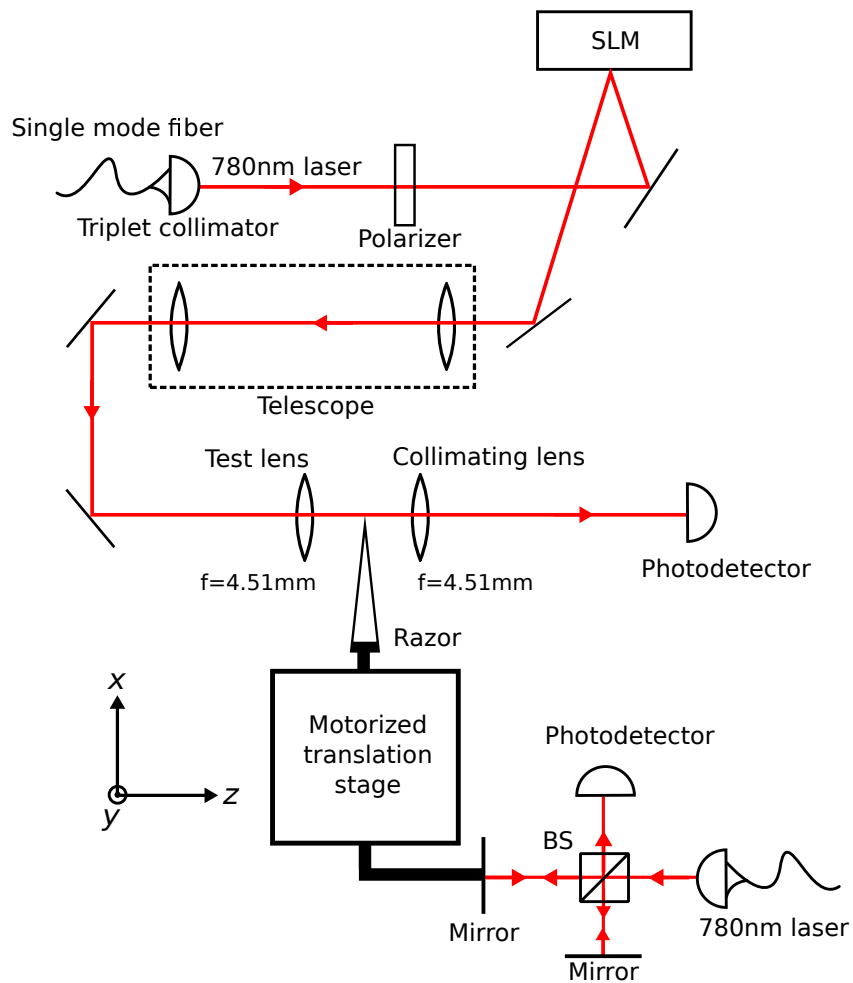


Figure 10: Optical setup to minimize beam waist with SLM and knife-edge measurement. A phase pattern is uploaded to the SLM to correct the wavefront errors. BS: Beamsplitter. SLM: Spatial light modulator.

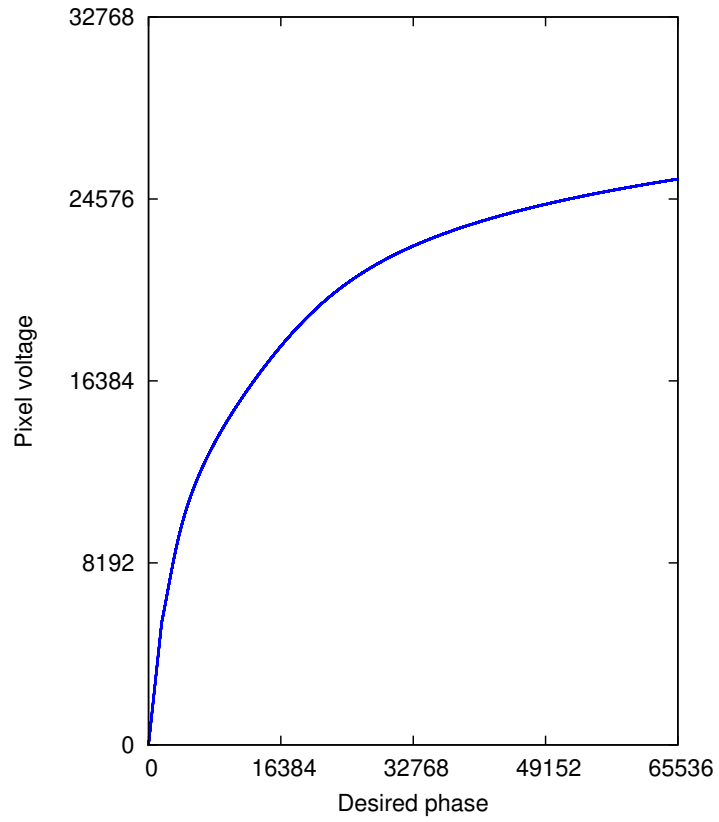


Figure 11: Relation between the pixel voltage and the desired phase. The conversion is done with a lookup table to linearize the output phase response ranging from 0 to 2π (0 to $2^{16} - 1 = 65535$).

4.2 Zernike Polynomials

We use Zernike polynomials (or Zernike modes) to express the phase patterns uploaded to the SLM, because they form an orthogonal basis on a unit disk and the lowest orders describe common phase patterns associated with typical lens aberrations [36]. Each of these Zernike modes is represented by two non-negative integer numbers $\{n, m\}$. There are two classes of Zernike modes: even and odd, which signify the cosine and sine dependence of the polar angle, respectively. We denote the even modes as Z_n^m , and odd modes as Z_n^{-m} . In polar coordinates, their expression is given by

$$\begin{aligned} Z_n^m(\rho, \phi) &= R_n^m(\rho)\cos(m\phi), \text{ (even modes)} \\ Z_n^{-m}(\rho, \phi) &= R_n^m(\rho)\sin(m\phi), \text{ (odd modes)} \\ R_n^m(\rho) &= \sum_{k=0}^{\frac{n-m}{2}} \frac{(-1)^k (n-k)!}{k! (\frac{n+m}{2} - k)! (\frac{n-m}{2} - k)!} \rho^{n-2k}, \end{aligned} \quad (12)$$

and where n, m satisfy $n \geq m$ and $m = n, n-2, n-4, \dots$ ($n-m$ must be even). To simplify the enumeration, we combine the two indices n and m to one single-index mode number j . The relation is given by

$$j = 1 + \frac{n(n+2) + m}{2}.$$

We also group the Zernike polynomials into different orders according to their spatial frequency. The order number of Zernike polynomials is given by the index number n with the order number $N_{order} = n + 1$; $n = 0$ is equivalent to $N_{order} = 1$. Larger order number of Zernike polynomials corresponds to higher spatial frequency. Polynomials from order 1 to order N_{order} are given by the first $N_{order}(N_{order} + 1)/2$ Zernike modes.

In general, the polynomials are used to describe common aberrations and misalignment such as tip, tilt, defocus, astigmatism, coma, and spherical aberrations [37, 38]. Table 3 contains information about the first six Zernike modes.

We begin with determining the position of the center of laser beam on the SLM screen (x_c, y_c) and the characteristic radius R_c ($R_c \simeq 2w_{in}$). The phase pattern used to drive the SLM is composed of the default surface correction phase mask and Zernike polynomials rescaled to a pixel area with a radius of R_c , corresponding to the beam that passes through the aperture of the focusing lens, i.e., $\rho = \sqrt{(x^2 + y^2)}/R_c$. The determination of x_c , y_c and R_c is further discussed in Section 7.1.

4.3 Waist Optimization

In order to correct for aberrations of the focusing lens, which are likely to be dominated by long-range deviations of its ideal phase transformation properties, a method needs to be applied to correct these deviations. This is where the Zernike polynomials become a useful basis.

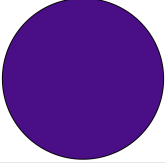
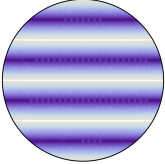
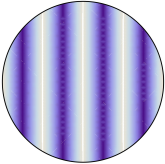
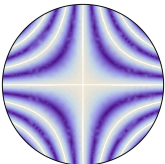
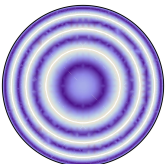
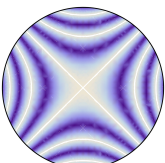
4.3.1 Gradient Search Algorithm

The additional phase mask Φ applied to the SLM can be expressed as a linear combination of different Zernike terms:

$$\Phi = \sum_{i=1}^N a_i Z_i, \quad (13)$$

where a_i is the weight of i -th Zernike mode. One has to take note that it is practically impossible to go through an infinite number of Zernike expansions. Besides,

Table 3: First six Zernike modes. The colour of phase pattern represents a phase of 0 (blue) to π (white).

Mode number j	$\{n,m\}$ indices	Polynomial	Aberration type	Phase visualization
1	$\{0,0\}$	1	Piston	
2	$\{1,-1\}$	$2\rho \sin\phi$	Vertical Tilt	
3	$\{1,1\}$	$2\rho \cos\phi$	Horizontal Tilt	
4	$\{2,-2\}$	$\sqrt{6}\rho^2 \sin 2\phi$	Oblique Astigmatism	
5	$\{2,0\}$	$3(2\rho^2 - 1)$	Defocus	
6	$\{2,2\}$	$\sqrt{6}\rho^2 \cos 2\phi$	Vertical Astigmatism	

the Zernike polynomials have a higher spatial frequency for larger indices while the lens aberrations are expected to be of low spatial frequency, it is reasonable to restrict the order of the Zernike polynomials for an optimal phase compensation to N terms.

Waist minimization is an optimization problem; we are looking for the optimal weights of each of the Zernike terms given by

$$\arg \min_{\{a_i\}_{i=1}^N} w(\Phi) .$$

We implemented a gradient search algorithm to vary the weights of Zernike modes one at a time. Here we choose the deterministic gradient descent for its simplicity. Assuming that the Zernike modes are decoupled, this algorithm also allows us to extract the contribution of each mode directly from the change in waist radius during the iterations. Implementation of stochastic optimization algorithms is possible to explore larger search space.

Our scheme can be summarized as follows:

1. Initialization: A knife-edge measurement is performed to measure the beam radius. A full measurement includes $n_x = 9$ single knife-edge cuts along x -direction (perpendicular to optical axis) at different z positions along the propagation direction. To speed up the optimization run, coarser step size of $\Delta x = 0.2 \mu\text{m}$ is applied. The smallest waist radius is recorded.
2. With the initial values of $a_i = 0$ for all $i \in [1, N]$, the weight is varied one by one starting from mode $i = 1$ to $i = N$ with a weight step size Δa of ± 0.2 in a unit of 2π phase. For each new weight, the waist is remeasured and recorded along with the best weights. The next iteration is based on the best weights of previous iterations.

3. Step two is repeated twice. When the search reaches the last mode $i = N$, the following iteration starts from mode $i = 1$ again.

The parameter N in the search algorithm is important because if N is too small, the SLM may not be able to compensate for certain aberrations; but if N is too large, which means higher search space dimension, it takes a longer time to complete the algorithm (one Zernike mode takes one minute in average). $N = 10, 21, 36, 45$ and 91 (correspond to Zernike modes up to order 4, 6, 8, 9, 13) are tested by comparing their convergence after two full cycles. We found that when $N \geq 36$, the algorithm converges to same waist after two full cycles, which implies that Zernike term Z_i is much less significant for $i > 36$. $N = 10$ and 21 do not reduce the waist as much as $N = 36$; thus we set $N = 36$ for the rest of this section. This choice is further discussed in Section 7.2.

4.3.2 Results and Discussions

Figure 12 shows the results of the gradient search optimization to minimize the beam radius for different focusing parameters u . All of the four optimization runs have the same behaviour: the waist radius reduces drastically within the first 10 iterations and then tapers off. The beam radius is close to convergence during the second cycle since the waist change is actually smaller than the fit error (iterations range between 37 and 72).

Beam radius and M^2 of the corrected beam for different focusing parameters u are also illustrated in Figure 14. Compared to Figure 12, the error bars in Figure 14 are much smaller because coarser step size of $\Delta x = 0.2 \mu\text{m}$ is applied during the iterations to speed up the optimization (while the beam radii in Figure 14 are measured with $\Delta x = 75 \text{ nm}$). The beam radius decreases significantly in all of the four cases, which demonstrates improved focusing with the SLM.

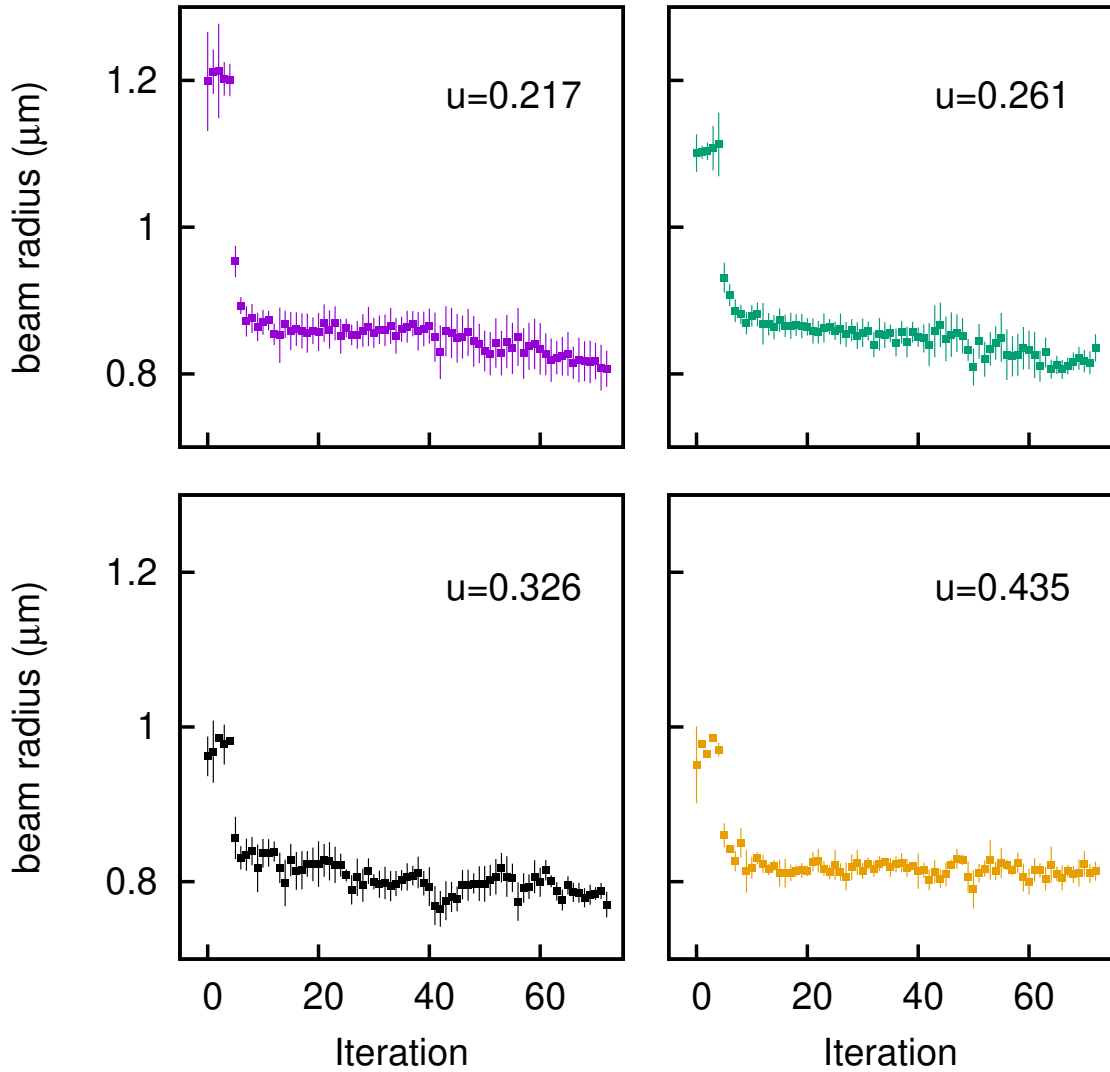


Figure 12: Optimized waist radius as a function of iteration steps. The initial waist radii are shown in Figure 8. Error bars represent one standard deviation of propagated fitting uncertainties.

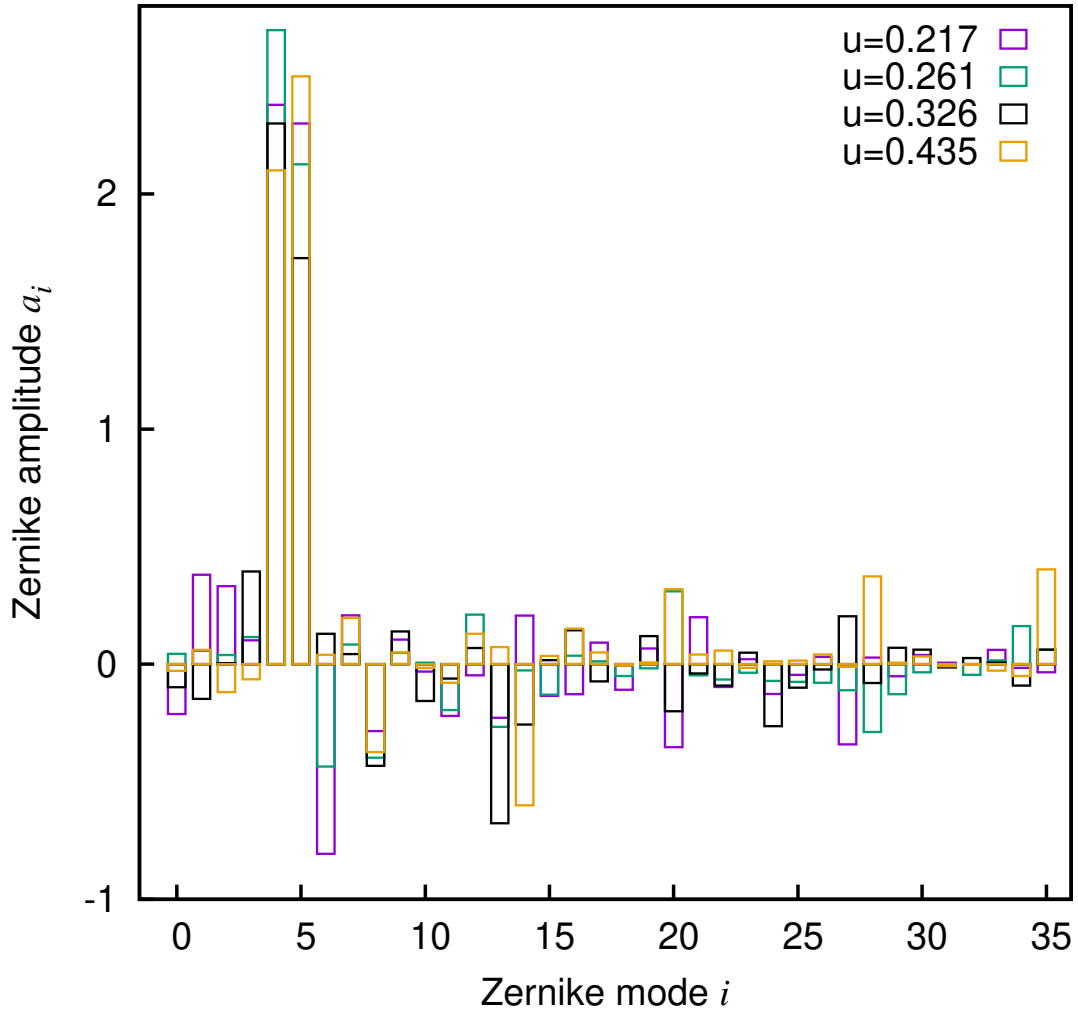


Figure 13: Zernike decompositions of the phase mask for different magnifications.

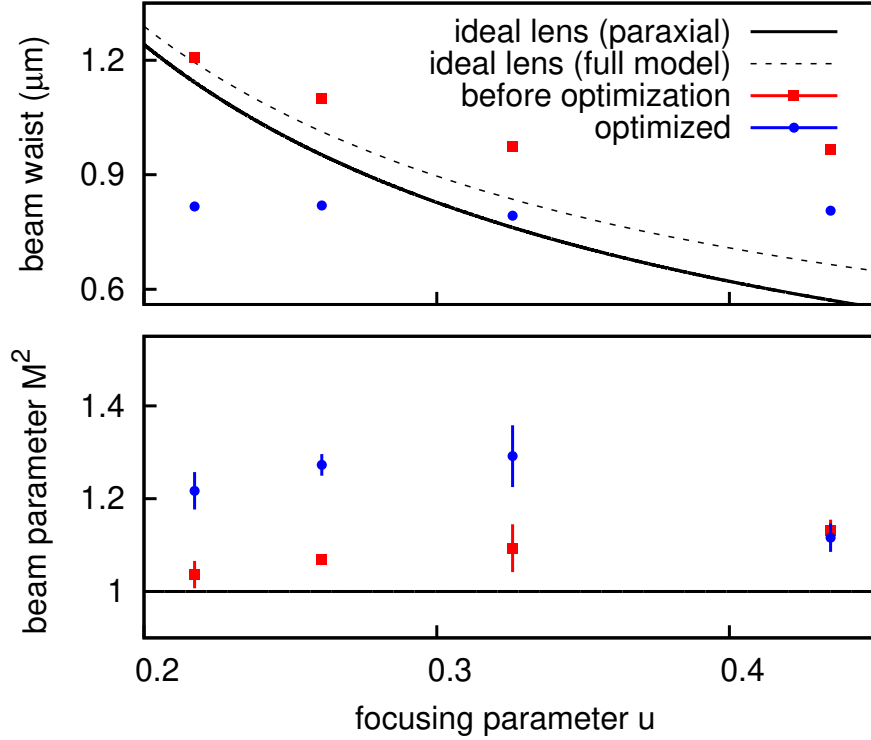


Figure 14: Waist radius and M^2 as a function of focusing parameter u . Black solid line: theoretical prediction for a collimated ideal Gaussian beam under paraxial approximation. Black dashed line: theoretical prediction for the full model described in [17]. Red dots: beam waists when SLM performs as a flat mirror (with no correction phase pattern uploaded). Blue dots: beam waists with optimization algorithm. Error bars represent one standard deviation of 10 repeated measurements. Error bars in the top panel are smaller than symbol size.

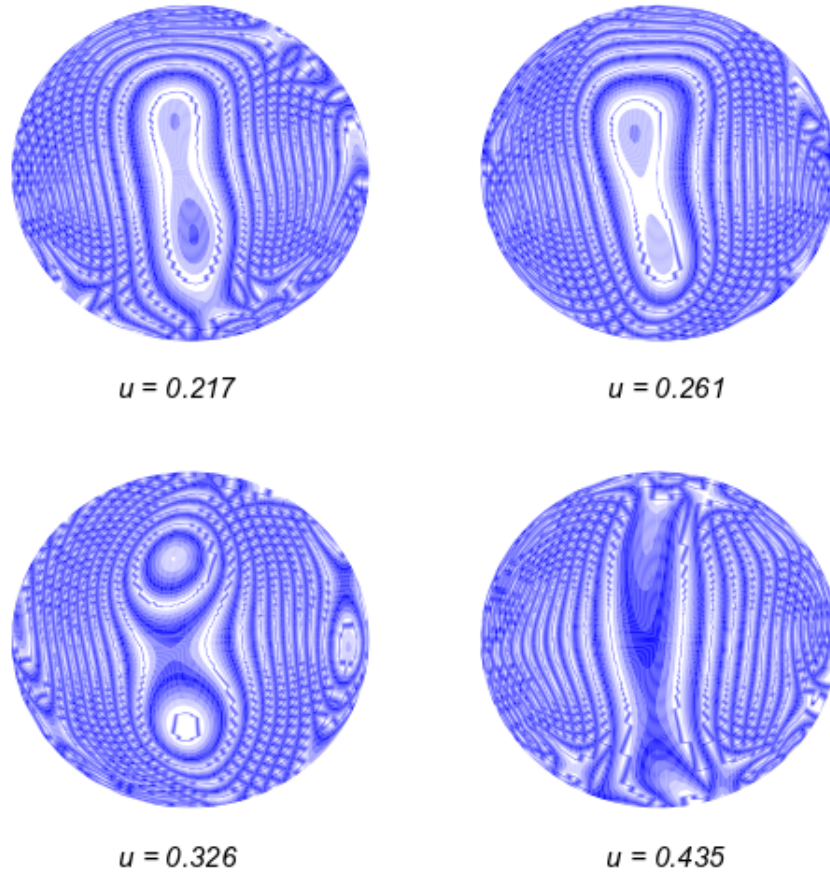


Figure 15: Contour plot of phase patterns that yield the smallest beam radius near focus at the end of optimization for different focusing parameters u . The colour represents a phase of 0 (white) to $\pm\pi$ (blue).

Here we observe two different optimization behaviours. For a magnification of 1.0 which corresponds to a focusing parameter u of 0.435, the beam radius is reduced while maintaining its Gaussian profile as M^2 stays rather close to 1.0. On the other hand, contrary to our expectation, for magnifications of 0.5 ($u = 0.217$) and 0.6 ($u = 0.261$), the algorithm does not yield optimized points near the black line which corresponds to theoretical prediction. The optimization scheme succeeded in reducing the waist radius for magnifications of 0.5 and 0.6 below the diffraction limit of a collimated Gaussian beam traversing ideal lens. The fairly large value of M^2 ($M^2 = 1.22 \pm 0.04$ for magnification of 0.5, $M^2 = 1.27 \pm 0.02$ for magnification of 0.6) suggests that the SLM deforms the Gaussian beam while minimizing beam radius. This postulate is also supported by Zernike decompositions of phase pattern applied onto the SLM, as plotted in Figure 13 for each focusing parameter u . The large amplitude for mode number 4 and 5, which correspond to the astigmatism mode and (de)focusing mode, indicates that the SLM modifies the beam divergence in order to obtain smaller beam radius at the focus. Besides, we notice that all the optimized beam radii values fall to similar values, that are around $0.8 \mu\text{m}$, for all focusing parameter u . We conjecture that this is due to the finite resolution of the SLM which has a pixel pitch size of $25 \times 25 \mu\text{m}$.

The optimized phase patterns for different focusing parameters u are shown in Figure 15. We observe that the spatial variation of the phase patterns is only significant in x -direction, since the optimization uses only the waist radius in x -direction at the focus as an optimization parameter. This implies that this method could only compensate for the lens error along the axis of optimization.

To confirm that the light intensity at the focal spot does increase at the end of optimization, we measure via the knife-edge method the intensity profile along x -direction reconstructed from the discrete gradient of photodiode reading (see

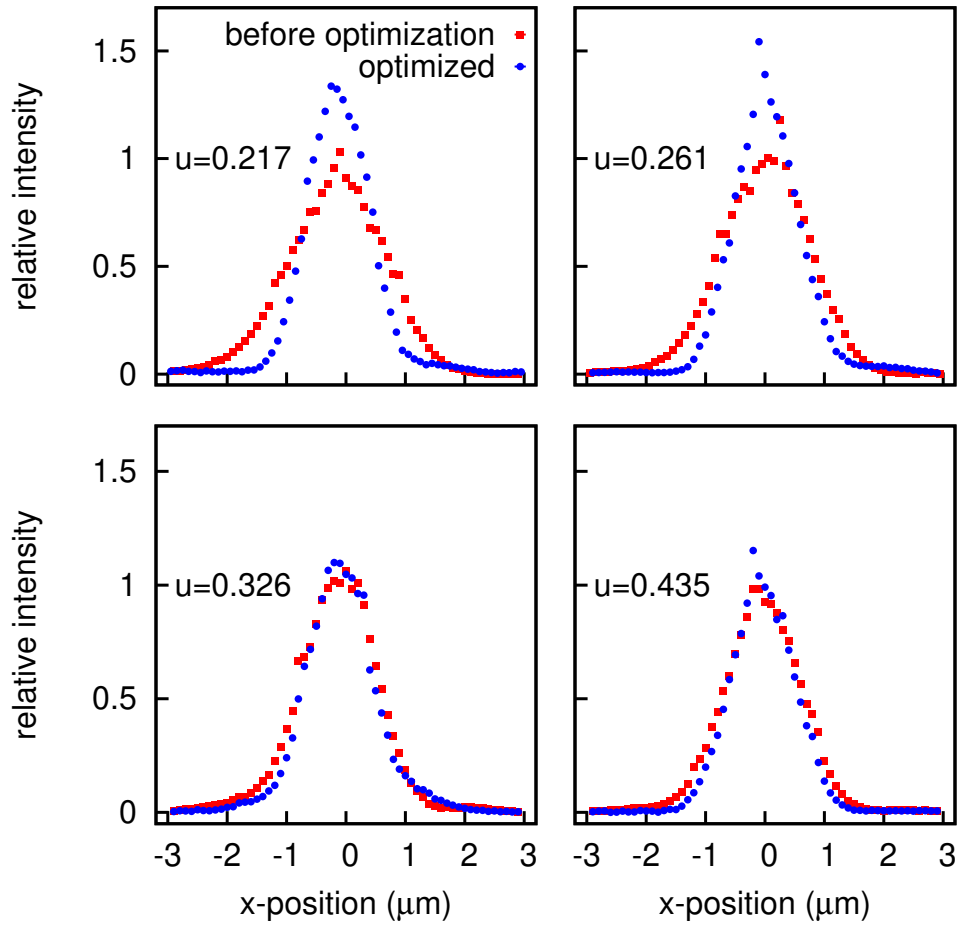


Figure 16: Intensity profile reconstructed from the discrete gradient of photodiode reading. The intensity is normalized with respect to the intensity peak of beam profile before optimization. Red dots: light intensity before the waist optimization. Blue dots: light intensity at the end of waist optimization. Error bars (smaller than symbol size) represent one standard deviation of 10 repeated measurements.

Section 4.4.1) with respect to x -position of the razor near the focal point. Figure 16 shows the intensity profile reconstructed for different magnifications. We observe that peak intensity increases by 30% for magnification = 0.5 and 0.6. For larger magnification, the improvement is less obvious (increase by 5%).

4.4 Intensity Optimization

4.4.1 Intensity Reconstruction

As shown in Section 4.3, it is possible to improve the focusing by manipulating the phase of the collimated laser beam before the focusing lens by using the beam radius at the focus as an optimization parameter. For the purpose of enhancing atom-light interaction, we are interested in the light intensity at the focal point instead of its distribution over the focal plane. This is because the atom-light interaction is determined by the product of the dipole moment and the electric field at the location of the atom, which can be considered point-like on the length scale of an optical wavelength for any focused light field. It is therefore natural to reconstruct the intensity distribution from transmitted power and maximize the peak intensity during an optimization run. Besides, we observed that the beam intensity distributions possess small side lobes in some runs. These undesired features could distort the error function fit and overestimate the beam waist.

To extract peak intensity from the knife-edge measurement, we reconstruct the intensity profile from finite differences of transmitted power given by

$$\begin{aligned} I(x) &\propto \frac{d}{dx}P(x) \simeq \frac{\Delta P(x)}{\Delta x} \\ &= I_0 e^{-2\left(\frac{x-x_0}{w}\right)^2}, \end{aligned} \tag{14}$$

where I_0 is intensity amplitude, x_0 is the center x -position, and w is the focal waist radius. In this expression, $P(x)$ is the transmitted power when the razor blade moves along the x -axis obtained from Eqn. 9.

In the next section, we describe a modified optimization scheme based on the maximization of the peak intensity of laser beam.

4.4.2 Experimental Setup

We employ the knife-edge technique with finer step sizes of $0.15 \mu\text{m}$ (as compared to $0.2 \mu\text{m}$ used in waist optimization) in the transverse direction so that the finite difference approximates the gradient with smaller errors. Lens errors give rise to side lobes in the intensity transverse profile which impact the fit to a Gaussian function. Figure 17 shows one such example. To avoid the side lobes, we use only a subset of the gradient data that lies within the range $\pm 0.45 \mu\text{m}$ around the peak, and fit them to Eqn. 14. Five of such Gaussian profile reconstructions are recorded at the intervals of $0.76 \mu\text{m}$ along the beam propagation direction centered around the focal point. One notices that the product $I(z)w(z)$ is constant because it is proportional to the optical power. A simplification is applied to Eq. 2 to obtain

$$I(z) = \frac{I_f}{\sqrt{1 + \left(\frac{z-z_0}{z_R}\right)^2}}, \quad (15)$$

where I_f is the peak intensity and z_0 is focal z -position. The Gaussian profile reconstructions are fit to Eq. 15 to give the peak intensity. Using the peak intensity as the optimization parameter, the optimization employs the same gradient search algorithm described in Section 4.3.1.

One should note that optical power drifts over time. It is therefore necessary to compare the light intensity at the focus relative to the total optical power incident on the aspheric lens at the same time. To achieve this goal, slight modifications are done to the knife-edge setup, as illustrated in Figure 18. We divide the beam into two paths with a beamsplitter: one is focused with the aspheric lenses for knife-edge measurement, the other is used to monitor the optical power. From this point onwards, we always refer relative intensity as the ratio of intensity measured after the aspheric lens to that before the aspheric lens.

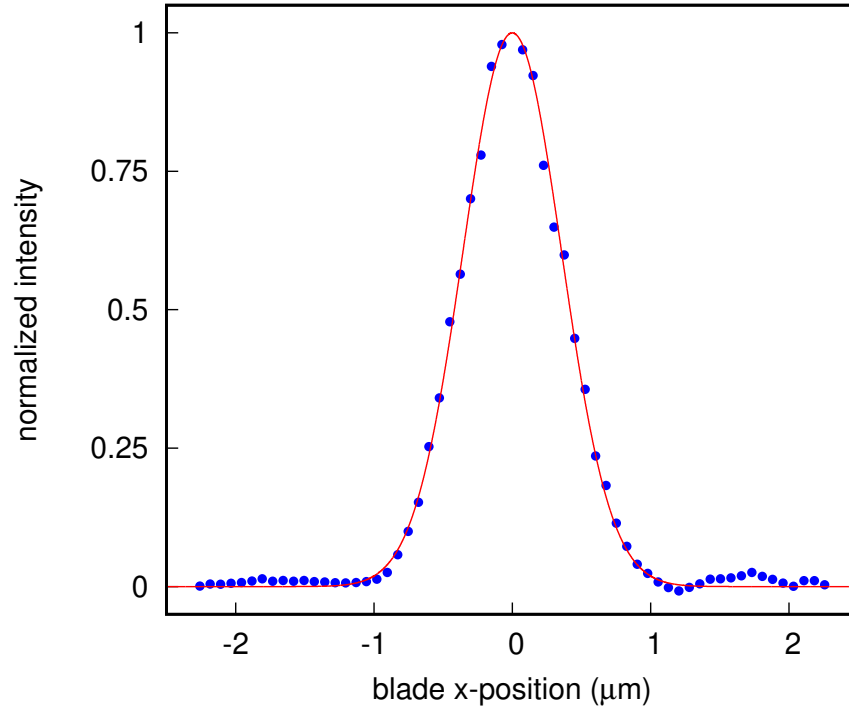


Figure 17: Intensity profile reconstructed from the discrete gradient of photodiode reading after optimization for focusing parameter u of 0.326, with a side lobe (3% amplitude with respect to the peak intensity) on the right side of the peak. The intensity is normalized to the peak intensity. Red line represents a fit to a Gaussian function. Error bars (smaller than symbol size) represent one standard deviation of 10 repeated measurements.

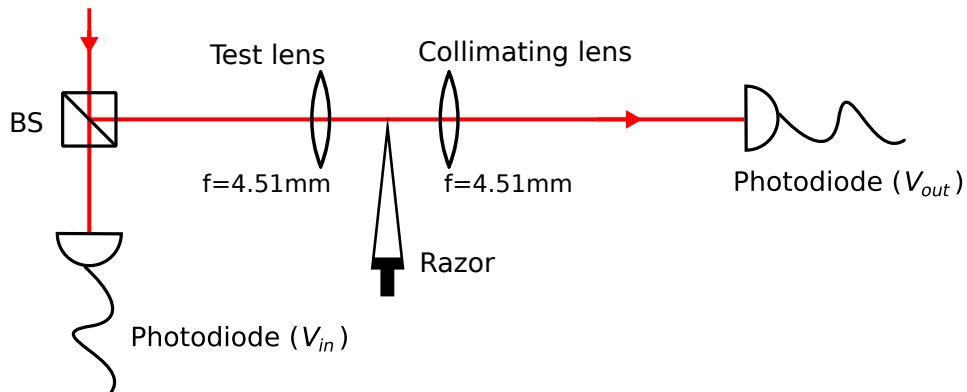


Figure 18: Simplified schematic depiction of the modified knife-edge measurement setup. A beamsplitter is added to measure the instantaneous beam power. Relative intensity refers to $\frac{dV_{out}}{dx}/V_{in}$. BS: Beamsplitter.

4.4.3 Results and Discussions

We applied the intensity optimization algorithm to the SLM for three different focusing parameters: $u = 0.217$ (magnification of 0.5), $u = 0.326$ (magnification of 0.75) and $u = 0.435$ (magnification of 1.0) of the incoming beam. Figure 19 shows the results of the optimization and the final Zernike amplitudes. We observe a similar behaviour during the convergence process: the relative intensity increases drastically within the first 10 iterations of low order Zernike modes. The relative intensity comes close to convergence during the second cycle with the intensity improvement being smaller than the fit error (iterations range between 37 and 72).

We have also put the settings back to the same initial values before the intensity optimization and started again with the waist optimization algorithm for comparison. At the end of optimization, the full beam profile (beam waist radius as well as M^2) and relative peak intensity are measured and are compared to the initial values. The summary of the results are shown in Figure 20. We observe that both optimization schemes managed to reduce the beam radius significantly. The intensity optimization algorithm yields a slightly larger beam waist than the waist optimization. For $u = 0.217$, once again the scheme has brought the waist radius below the diffraction limit of a collimated paraxial beam traversing an ideal lens. On the other hand, the reconstructed relative peak intensity for both waist optimization and intensity optimization are fairly similar despite the small difference in beam waist. In terms of beam quality factor M^2 , we see the same behaviour as observed previously for the waist optimization algorithm: for smaller focusing parameters ($u = 0.217$ and $u = 0.326$), there is a trade-off between beam quality factor and smaller beam waists. For $u = 0.435$, M^2 value is unusually large compared to the value obtained previously. From Figure 19, we see that the

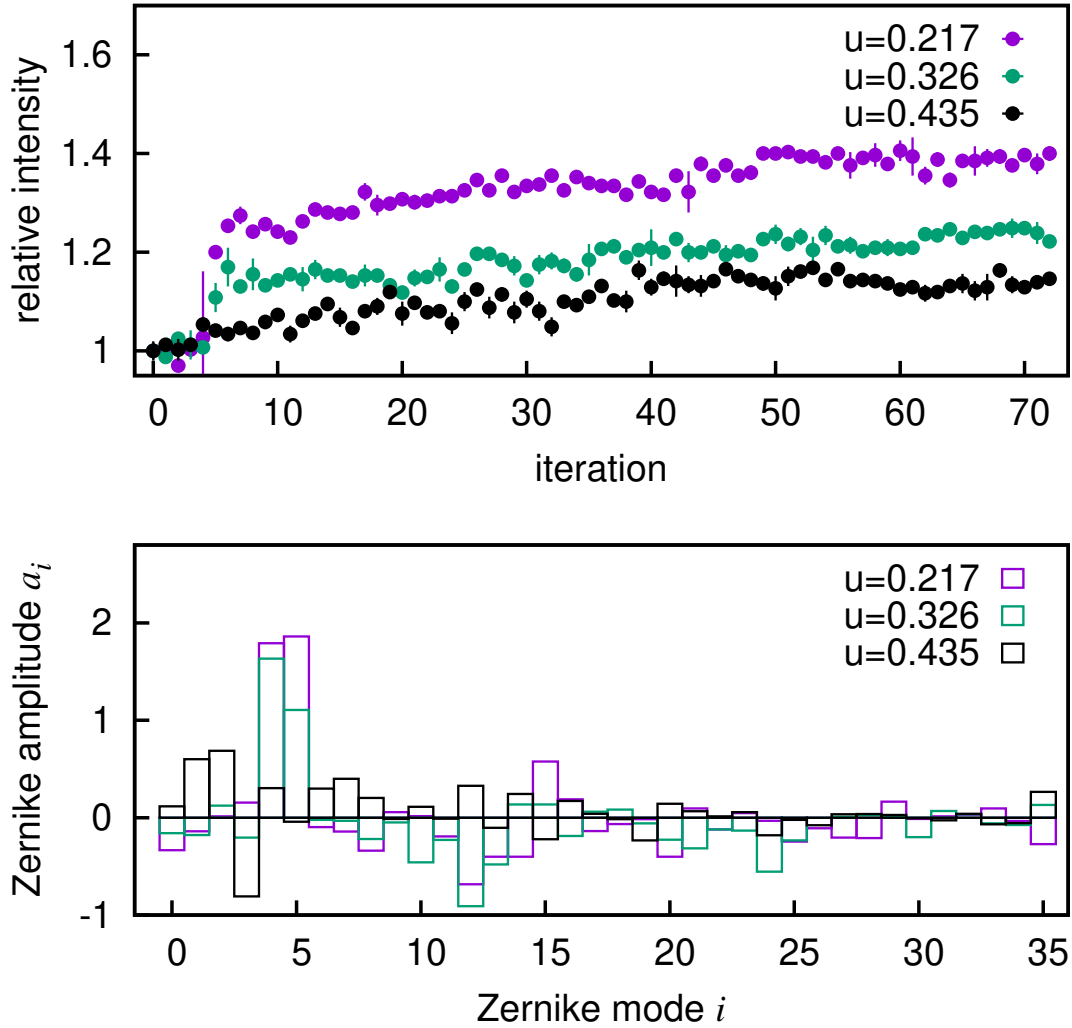


Figure 19: Top: optimized relative intensity as a function of iteration steps. The relative intensity has been normalized to the initial relative intensity. Error bars represent one standard deviation of propagated fitting uncertainties. Bottom: Zernike decompositions of the phase mask.

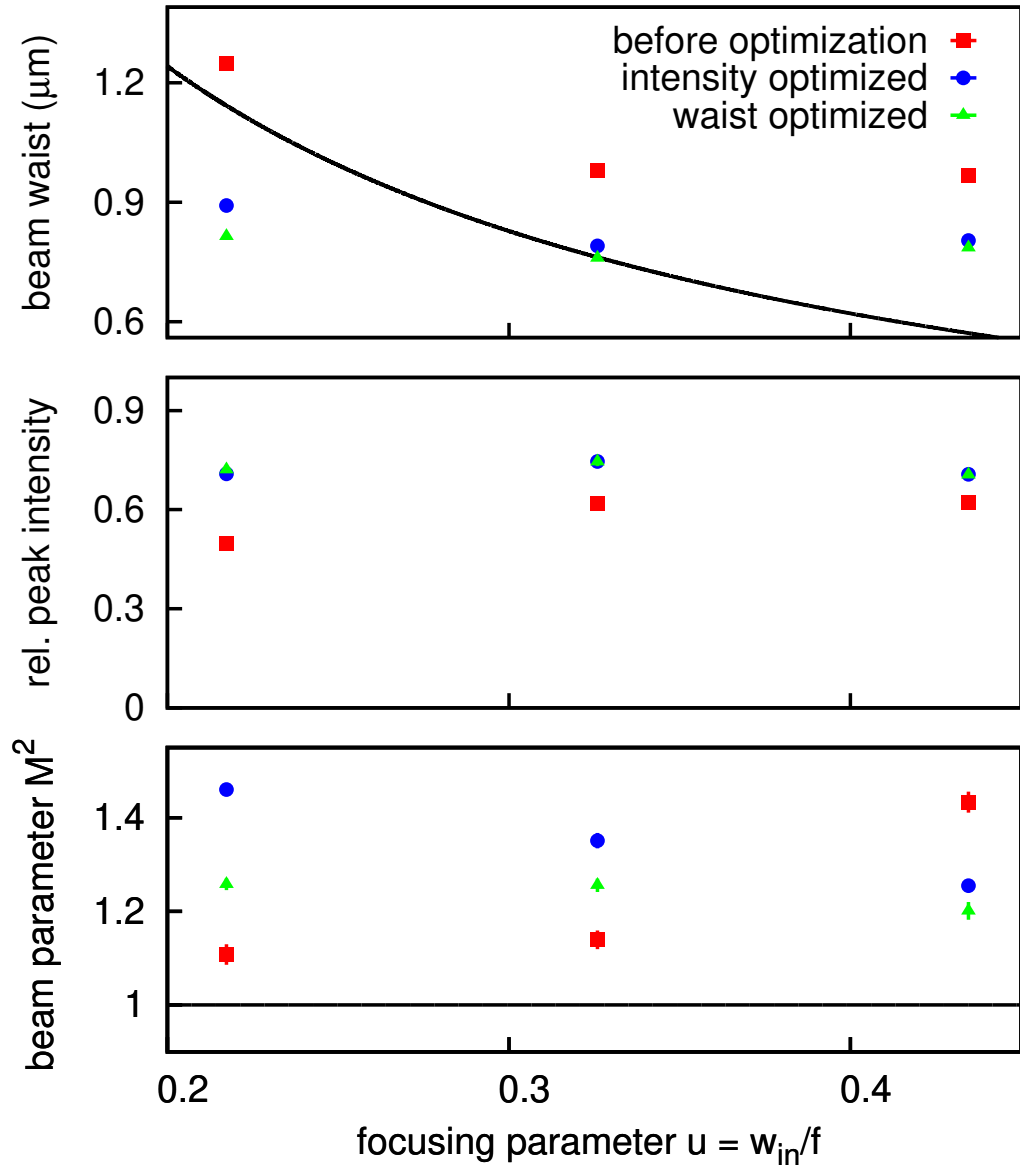


Figure 20: Plot of beam radius, peak relative intensity and M^2 as a function of focusing parameter u . Black solid line: theoretical prediction for a collimated ideal Gaussian beam. Red dots: beam waists when the SLM performs as a flat mirror (with no correction phase pattern uploaded). Blue dots: beam waists with intensity optimization algorithm. Green dots: beam waists with waist optimization algorithm. Error bars represent one standard deviation of 10 repeated measurements. Error bars in the top two panels are smaller than symbol size.

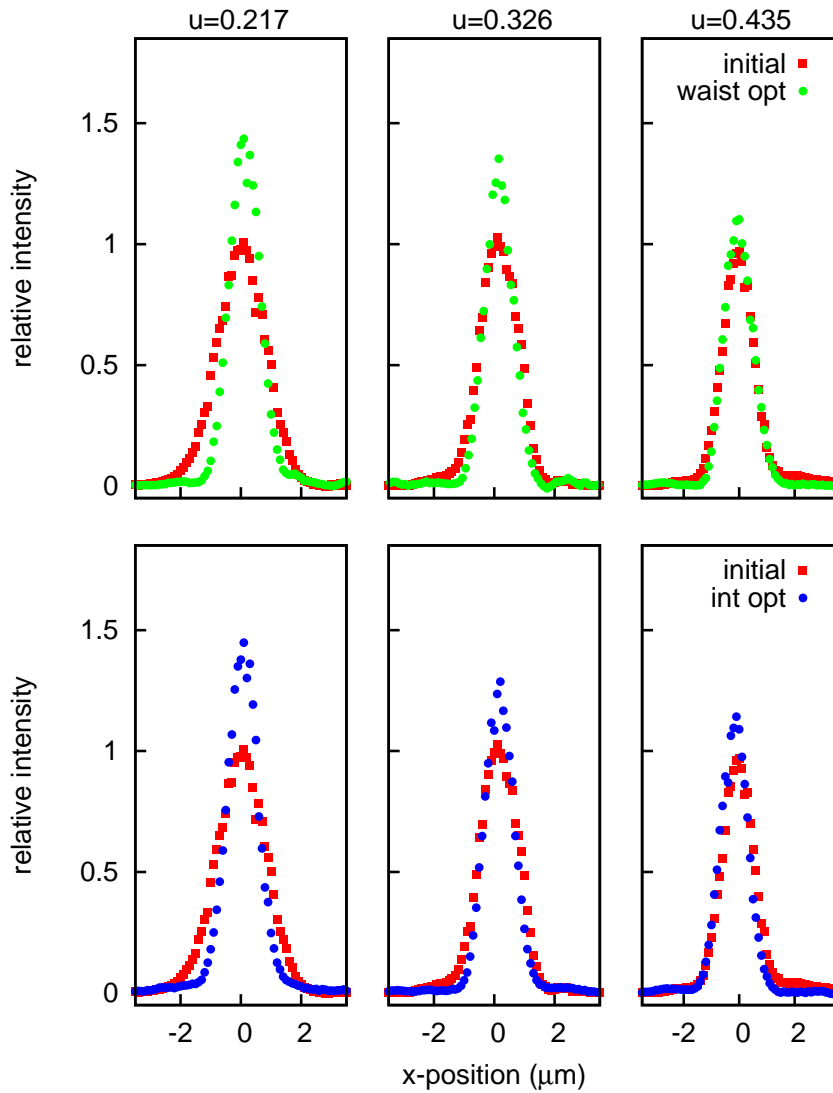


Figure 21: Relative intensity profile reconstructed from the discrete gradient of photodiode reading. Top three panels compare the relative intensity between waist optimization and uncorrected focusing optics. Bottom three panels compare the relative intensity between intensity optimization and uncorrected focusing optics. The focusing parameter u is 0.217 (left), 0.326 (middle) and 0.435 (right). The intensity is normalized with respect to the peak of relative intensity profile before optimization. Both optimizations seem to give a better improvement for small u . Red dots: light intensity before the waist optimization. Blue dots: light intensity at the end of intensity optimization. Green dots: light intensity at the end of waist optimization. Error bars (smaller than symbol size) represent one standard deviation of moving average.

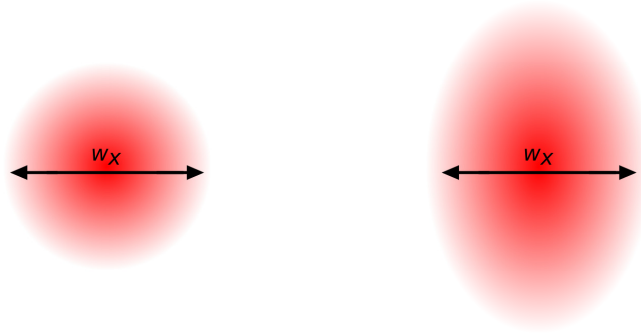


Figure 22: Transverse beam profiles having the same w_x but different w_y . One dimensional optimization based on w_x cannot distinguish these two transverse cross-sections.

Zernike amplitudes for mode 2 and 3 are more significant for $u = 0.435$ compared to smaller u values, which indicates that the initial settings could be slightly off for $u = 0.435$, leading to larger M^2 value.

With the optimized phase mask uploaded on the SLM, the reconstructed intensity profile along x -direction is reconstructed for both schemes, as shown in Figure 21. We sample the transmitted optical power at intervals of 75 nm over a range of 8 μm . To smoothen the graph, we plot the moving average of the reconstructed intensity over every 20 points. The improvement in peak intensity is 42 %, 20 % and 14 % for $u = 0.217$, 0.326 and 0.435, respectively.

In conclusion, both waist optimization and intensity optimization produce similar results and lead to improved focusing with the SLM. One drawback on this approach is that the knife-edge measurement only measures the beam radius along one axis. Since we do not implement any constraint on the other axis, the beam radius along the other axis may not reduce. In other words, the algorithm squeezes the beam in the direction of optimization but expands in the other. One example is shown in Figure 22. To investigate this hypothesis, we generalize this idea to obtain a two-dimensional optimization scheme.

5 Two-dimensional Optimization

5.1 Two-dimensional Knife-edge Method

The spatial structure of a focused laser beam can only be fully characterized by the one-dimensional knife-edge technique described earlier if the laser beam possesses cylindrical symmetry. In practice, a laser beam can be elliptical, and thus the knife-edge measurement in one single transverse direction is not sufficient to describe the focal beam spot area. Similarly, lens errors do not need to have rotational symmetry.

Taking the one-dimensional optimized beam transverse profile based on the intensity optimization algorithm described in Section 4.4 as an example, for a magnification of 1.0, the beam radius in the x -axis is reduced from $0.97 \pm 0.02 \mu\text{m}$ to $0.79 \pm 0.02 \mu\text{m}$ after correction. To investigate the change in beam radius in y -direction, we rotate the blade after optimization in x to perform the knife-edge measurement in the y -axis. We observe that the beam radius in the y -axis measured in one run (initialized at $w_y = 1.02 \pm 0.02 \mu\text{m}$) for repeated intensity optimization runs ranges from $0.9 \mu\text{m}$ to $1.5 \mu\text{m}$, which indicates that the phase mask for the optimization algorithm in the x -direction could negatively influence the beam radius in the transverse y -direction. From this we conclude that the one-dimensional optimization scheme does not necessarily reduce the focal beam spot area. Therefore, we seek to characterize the beam profile based on beam radii in two transverse orthogonal directions.

Table 4: Measured beam radii in transverse directions for three intensity optimization runs in x -direction at same initial setting.

	Initial	Run 1	Run 2	Run 3
w_x (μm)	0.97 ± 0.02	0.79 ± 0.02	0.80 ± 0.02	0.79 ± 0.02
w_y (μm)	1.02 ± 0.02	0.96 ± 0.02	1.30 ± 0.04	1.42 ± 0.04

A few approaches to characterize the transverse beam profile have been proposed and demonstrated in the literature. Some in-situ measurements involve the fabrication of straight knife-edges on two sides. Naber first succeeded to fabricate a tetrahedral tip (T tip) that can be used for knife-edge measurement [39]. The idea is to form an ultra-sharp common corner (T tip) by breaking off a piece of glass from a cover slide such that the tip has three orthogonal edges. The edges of these glass fragments are reported to have a radius of curvature of about 5 nm. By applying the same concept, Xie et al. constructed a double knife-edge device from a polished silicon wafer [40]. A silicon wafer is opaque to 780-nm light. By breaking the wafer twice successively along the symmetry axes without touching the fracture edges, the fracture edges which encloses a 90° angle can lead to an ultra-sharp tip. The other method is based on nanoparticle scanning [41]. This approach uses a single fluorescent nanoparticle as a probe to detect the intensity distribution in the focal plane of an objective.

Here, we take a simple approach. We constructed a compound knife that is capable of measuring the laser beam waist along two orthogonal transverse directions. We assembled two surgical scalpels (Scalpel Number 22, Hallmark Surgical) to form a L-shape blade. One could attach one scalpel on top of the other perpendicularly, but in this case the two blades would not be coplanar and their offset in the propagation direction of the beam would be on the order of the thickness of a scalpel (a few millimetres). Consequently, the piezo cannot access the beam radii of both directions at same z -location, since the maximum travelling range of the piezo is around $100\ \mu\text{m}$. To solve this problem, we grind the tip of one scalpel flat and attach this new flat edge to the blade of the other scalpel so that the two blade planes lie in the same transverse plane. After several trials, we obtained a working compound knife of which the distance between the

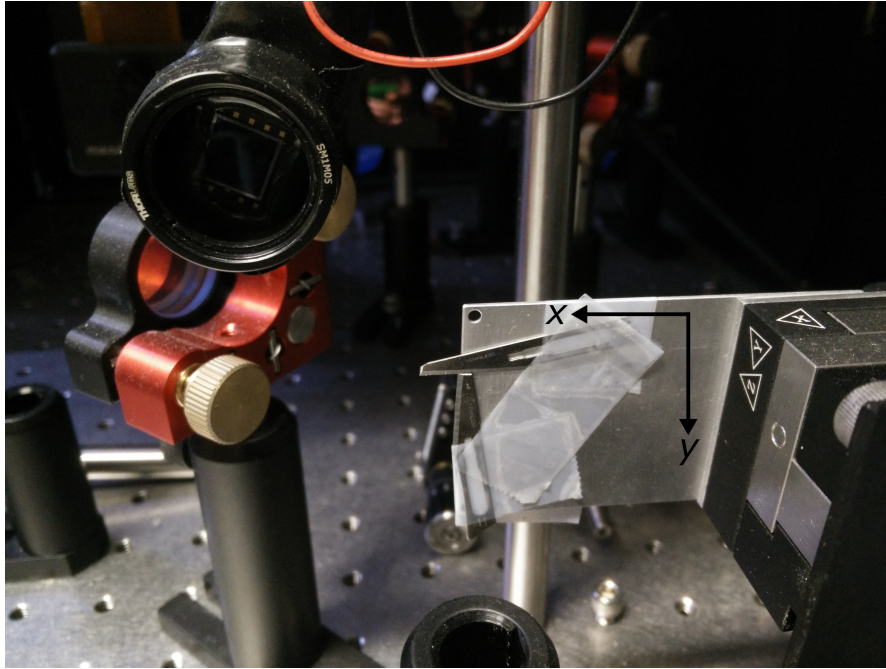


Figure 23: Photograph showing the compound knife consisting of a pair of orthogonally attached scalpels that measures the beam radii in the x and y directions based on knife-edge method.

two blade planes is determined to be around $31 \pm 1 \mu\text{m}$ (see Figure 23) that is calibrated by comparing the z offset of the x and y minimum beam radii .

5.2 Validity of the Measured Area

We assume that the laser beam has an elliptical Gaussian envelope in X and Y directions, described by beam waists w_X (semi-major axis) and w_Y (semi-minor axis).

Since the optical power flowing through the focal plane is conserved, in order to maximize the beam intensity, we need to minimize the transverse area of the laser beam. The contour of the beam waist radius can be described by $\frac{X^2}{w_X^2} + \frac{Y^2}{w_Y^2} = 1$, where (X, Y) represents focal plane basis defined by the elliptical axes. The elliptical cross-sectional area is then given to be $\pi w_X w_Y$.

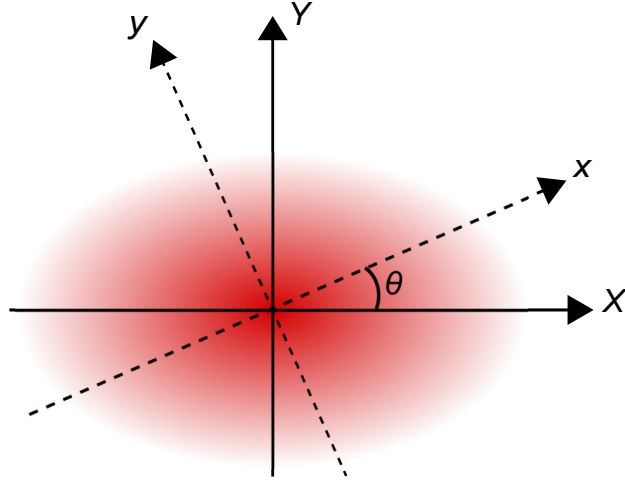


Figure 24: Elliptical cross-section of laser beam. The semi-major and semi-minor axes are aligned along (X, Y) . The knife-edge transversal basis (x, y) is assumed to be rotated counterclockwise through an angle θ with respect to (X, Y) .

In practice, the two major axes and the measurement axes do not coincide. Figure 24 shows one such example. Here, (x, y) represents the knife-edge transversal basis that is rotated away from the elliptical axes.

We let θ denote the angular tilt between the two bases, the coordinate transformation follows

$$\begin{aligned} X &= x \cos\theta - y \sin\theta \\ Y &= y \cos\theta + x \sin\theta, \end{aligned} \tag{16}$$

and the transmitted power measured by knife-edge technique along x -axis is given by

$$\begin{aligned} P_x &\propto \int_{-\infty}^x \int_{\mathbb{R}} \exp\left[-2\left(\frac{X^2}{w_X^2} + \frac{Y^2}{w_Y^2}\right)\right] dx dy \\ &= \int_{-\infty}^x \int_{\mathbb{R}} \exp\left[-2\left(\frac{(x \cos\theta - y \sin\theta)^2}{w_X^2} + \frac{(y \cos\theta + x \sin\theta)^2}{w_Y^2}\right)\right] dx dy \\ &\propto \int_{-\infty}^x \exp\left[-2\left(\frac{x^2}{w_X^2 \cos^2\theta + w_Y^2 \sin^2\theta}\right)\right] dx. \end{aligned} \tag{17}$$

It shows that measurement in blade basis still takes the form of an error function, with beam waist (in x -direction) $w_x = \sqrt{w_X^2 \cos^2\theta + w_Y^2 \sin^2\theta}$. Similarly, for a knife-edge measurement performed in y -direction, we obtain $w_y = \sqrt{w_Y^2 \cos^2\theta + w_X^2 \sin^2\theta}$.

One can show that

$$w_x^2 w_y^2 = w_X^2 w_Y^2 + \frac{\sin^2 2\theta}{4} (w_X^2 - w_Y^2)^2. \quad (18)$$

Our estimation is always larger or equal to the real cross sectional area $\pi w_X w_Y$, with the maximum estimation error bounded by $\pi \frac{(w_X^2 - w_Y^2)}{2}$. For the case of $w_X = w_Y$, the cross section of the laser beam is circular and our estimation is equal to the real cross sectional area.

5.3 Experimental Setup

For this experiment, we focus only on the case where focusing parameter is the greatest ($u = 0.435$, magnification = 1.0) as this provides the tightest focus to maximize atom-light interaction. In order to avoid additional aberrations and to simplify the setup, we remove the telescope, as shown in Figure 25. We also remove the collimating lens after the knife, which is used only for laser alignment purposes. To measure the transmitted optical power, we place a photodetector right after the compound knife.

Alignment procedure

Since the initial beam radius affects the convergence speed of an optimization run, we follow a set of alignment steps in order to obtain the same starting point.

To ensure that the laser beam hits the center of the test lens, we first try to maintain the roundness of the beam spot after passing through the aspheric lens.

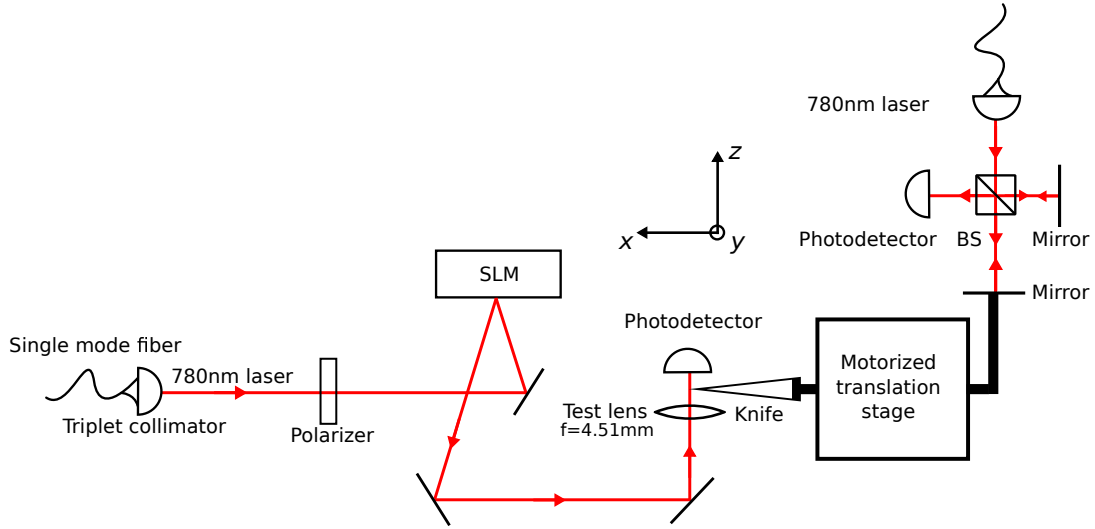


Figure 25: Optical setup to minimize beam waists in the x and y directions with SLM and 2-D knife-edge measurement. A phase pattern is uploaded to the SLM to correct the wavefront errors. The compound knife translates in x and y directions to measure beam radii w_x and w_y . BS: Beamsplitter. SLM: Spatial light modulator.

We use a second aspheric lens that is confocal to the test lens to recollimate the beam and monitor the recollimated beam spot shape. As shown in Figure 26, we adjust the beam direction and position on the test lens via the two mirrors before the aspheric lenses so that the beam spot exiting the collimating lens approximates a Gaussian transverse profile.

We then translate the compound knife. To define a consistent coordinate for the piezo stage, we manually move the compound knife in x and y directions to slightly crop the beam with its inner corner by tuning the translation stage and set this position to be $(x = 50 \mu\text{m}, y = 50 \mu\text{m})$. In this setting, the blade position $(x = 0 \mu\text{m}, y = 0 \mu\text{m})$ corresponds to being fully open (all light can be transmitted through) and $(x = 70 \mu\text{m}, y = 70 \mu\text{m})$ corresponds to being fully closed (no light passes through). While ensuring that the distance between the two blade planes are fixed, we program a single knife-edge cut to include a cut along both transverse

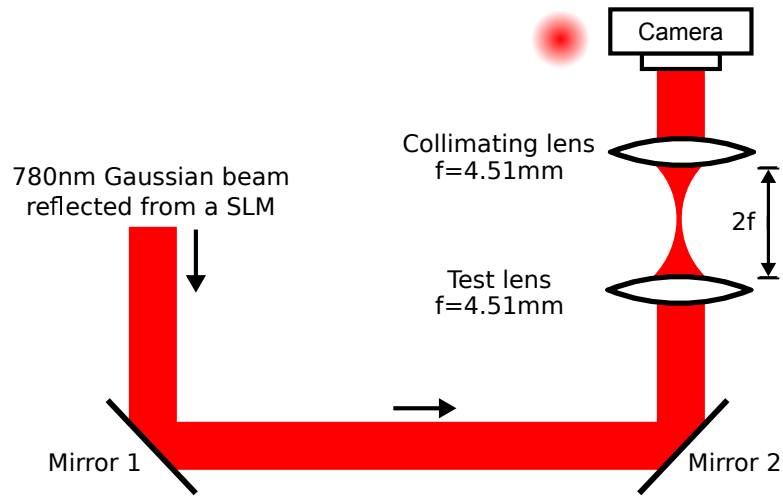


Figure 26: To ensure that the laser beam hits the center of the test lens, the recollimated beam leaving the collimating lens is monitored with a camera. Mirror 1 and mirror 2 are adjusted so that the beam spot exiting the collimating lens approximates a Gaussian transverse profile.

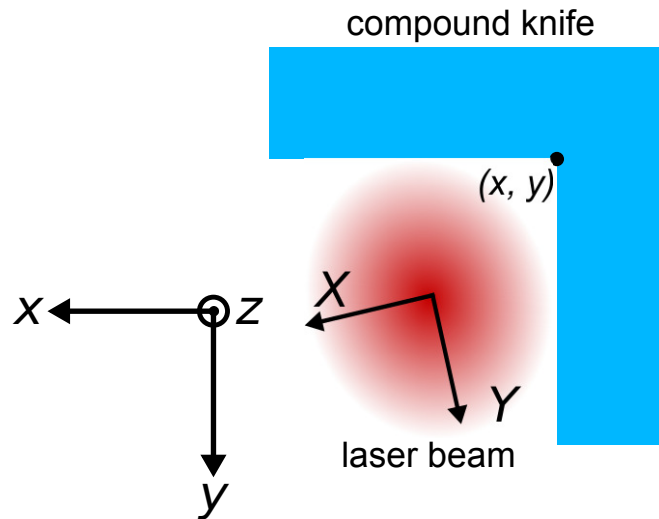


Figure 27: Laser beam transverse cross-section on the focal plane. In current setting, the coordinate of the compound knife's corner (x, y) is set such that all light can be transmitted through. We vary x (y) for a fixed $y(x)$ -position to obtain the beam radius in $x(y)$ -direction. (X, Y) corresponds to the principal axes of the elliptical beam.

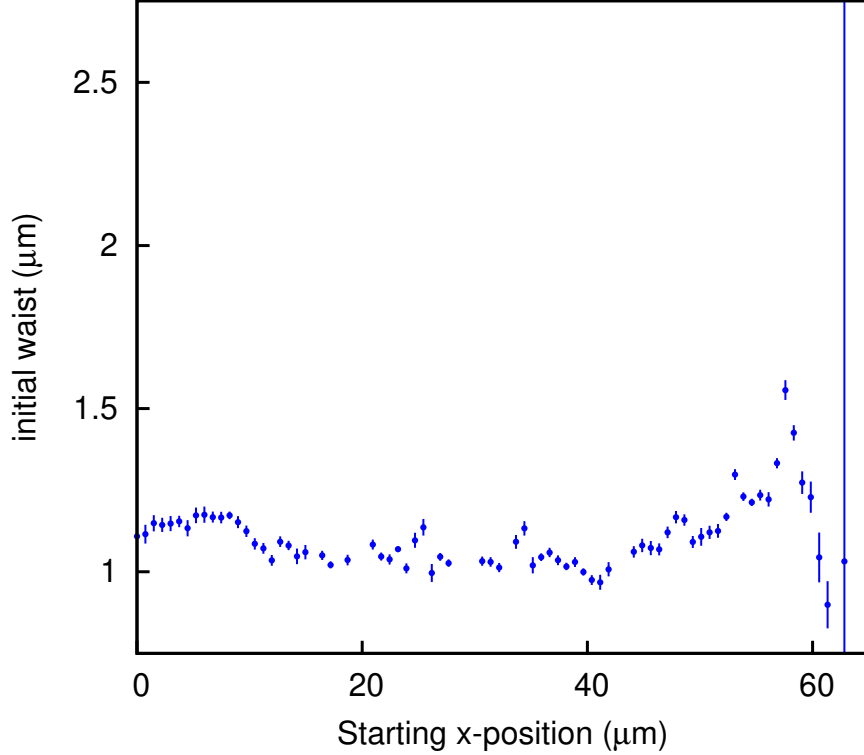


Figure 28: Beam radius in the y direction w_y with the knife edge at different x -positions. Error bars represent one standard deviation of propagated fitting uncertainties. When the blade position is larger than $50 \mu\text{m}$, the corner effect starts to intervene. The large uncertainty for position larger than $60 \mu\text{m}$ signifies clipping from the non-measuring scalpel.

x and y directions at intervals of 75 nm for a range of $10.6 \mu\text{m}$. Consequently, we minimize the beam quality factor M^2 in two transverse directions by fine-tuning the beam direction and position.

Due to the variation of the edge sharpness of the blade, we vary the blade locations (x, y) to obtain the best initial beam radii by manipulating the initial position of the knife. Figure 28 shows the influence of different starting points on the measured beam waist radius.

Optimization Scheme

We restate the optimization problem as

$$\text{minimize } w = \sqrt{w_x w_y}. \quad (19)$$

The area is then given by $A = \pi w_x w_y = \pi w^2$, where w is the geometric mean of w_x and w_y .

At the early stage of the experiment, from $1.00 \pm 0.01 \mu\text{m}$ the area optimization successfully reduced the geometric mean waist to $0.85 \pm 0.01 \mu\text{m}$, which corresponds to an improvement of 15% in waist reduction compared to the initial beam radius. However, with the phase mask obtained from the area optimization, the reconstructed peak intensity yields only about a 5% improvement for both transverse axes. Further investigation shows that during the optimization run, the SLM changes the divergence of laser beam slightly, which increases the clipping κ and decreases the transmitted power through the lens. This is especially significant for our chosen focusing parameter $u = 0.435$, the incident beam waist is comparable with the clear aperture of the aspheric lens ($\kappa = 3.5\%$). This is consistent with an observation in microscopy that overfilling apertures for confocal microscopy helps to focus light to a smaller focal spot size [42].

In order to compensate for the power drop due to the change in beam divergence, we modify the optimizing signal by multiplying the ratio of transmitted power to incident power as a weight,

$$\text{minimize } \tilde{w} = \frac{\sqrt{w_x w_y}}{P_{\text{trans}}/P_{\text{in}}}, \quad (20)$$

\tilde{w} represents the weighted geometric mean of waist radii.

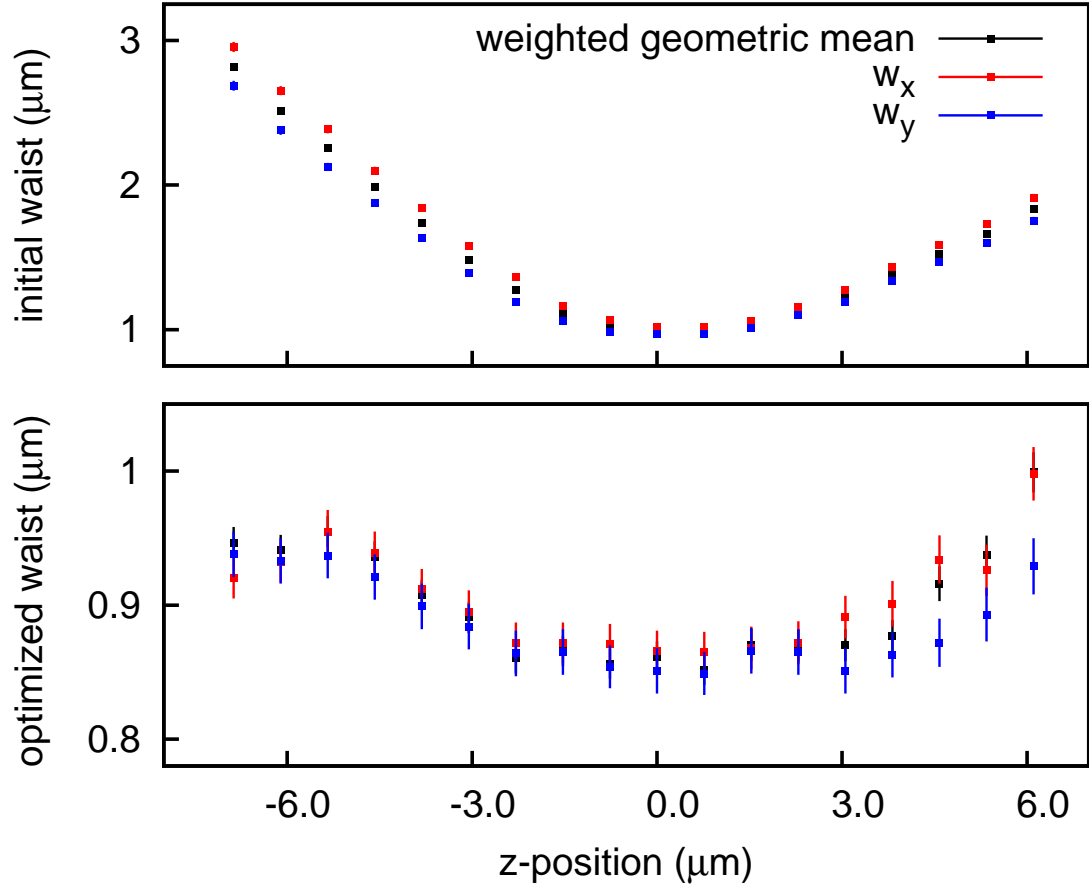


Figure 29: Optimization of beam waist at different z positions. Red dots: waist data measured along x -axis. Blue dots: waist data measured along y -axis. Black dots: geometric mean of w_x and w_y weighted with the relative power of the transmitted beam. Error bars represent one standard deviation of propagated fitting uncertainties. Error bars in top panel are smaller than symbol size.

Our new optimization scheme can be summarized in the following way:

1. Move the razor to a fixed z -position close to the focus.
2. Measure the initial \tilde{w} with two-dimensional knife-edge method.
3. Iterate over Zernike modes ($N = 36$) for two cycles to minimize \tilde{w} .
4. Repeat from step 1 at different z -positions.

5.4 Results and Discussions

Figure 29 summarizes the results of the area optimization at different z -positions. The initial beam radii as the z -position is varied along the focus are shown in the top panel. At each z -position, an area optimization run is applied once to minimize the weighted geometric mean of waist radii. Points in bottom panel at the same z -position then correspond to the optimized beam radii. We observe that there is a local minimum for the optimized beam waist, which stays close to the original focus. This is due to the fact that we are using an aspheric lens that is designed to minimize spherical aberration.

As seen in Figure 29, the area optimization algorithm gives the smallest beam radii at the focus $z = 0$. We then set $z = 0$ and study the beam profile corresponding to this optimization run. The optimization and Zernike amplitudes after minimizing the beam spot are shown in Figure 30. The beam waists along the two axes follows a slow decline during the first cycle. The waist radii were initialized at $1.02 \mu\text{m}$ (1.31λ) and $0.97 \mu\text{m}$ (1.24λ) in x and y directions; they were both optimized to 850 nm (1.09λ). One sees an abrupt drop in beam waist at the iteration 41 (related to Zernike mode 5). We hypothesize that the (de)focusing mode (Zernike mode 5) is the dominant aberration mode. The difference in beam

waists between two axes also decreased from 90 nm to 10 nm, resulting in smaller ellipticity of the optimized beam at the focus.

We observe an improvement of 17% and 12% in beam radii for the x and y transverse axes, respectively. To confirm that the intensity is also improved, we reconstruct the intensity profile at the focus before and after the area optimization, as illustrated in Figure 31. A fit to a Gaussian function is performed on the reconstructed intensity data around the peak ($\pm 0.61 \mu\text{m}$) to obtain the peak intensity. We observe an intensity improvement of 17.6% (x -axis) and 16.3% (y -axis).

Furthermore, we measure the full transverse beam profile at the focus with the best phase mask obtained with area optimization at the focus. The result is compared with the beam profile without optimization in Figure 32. This shows that the focal point does not change after optimization. This might be due to the fact that an aspheric lens is designed to have minimum spherical aberrations. Besides the improvement in beam waist radii, M^2 is also reduced from 1.38 ± 0.02 to 1.224 ± 0.005 (x -axis) and from 1.16 ± 0.04 to 1.03 ± 0.01 (y -axis). This implies that after the area optimization run, the transverse beam profile approximates better an ideal Gaussian transverse profile.

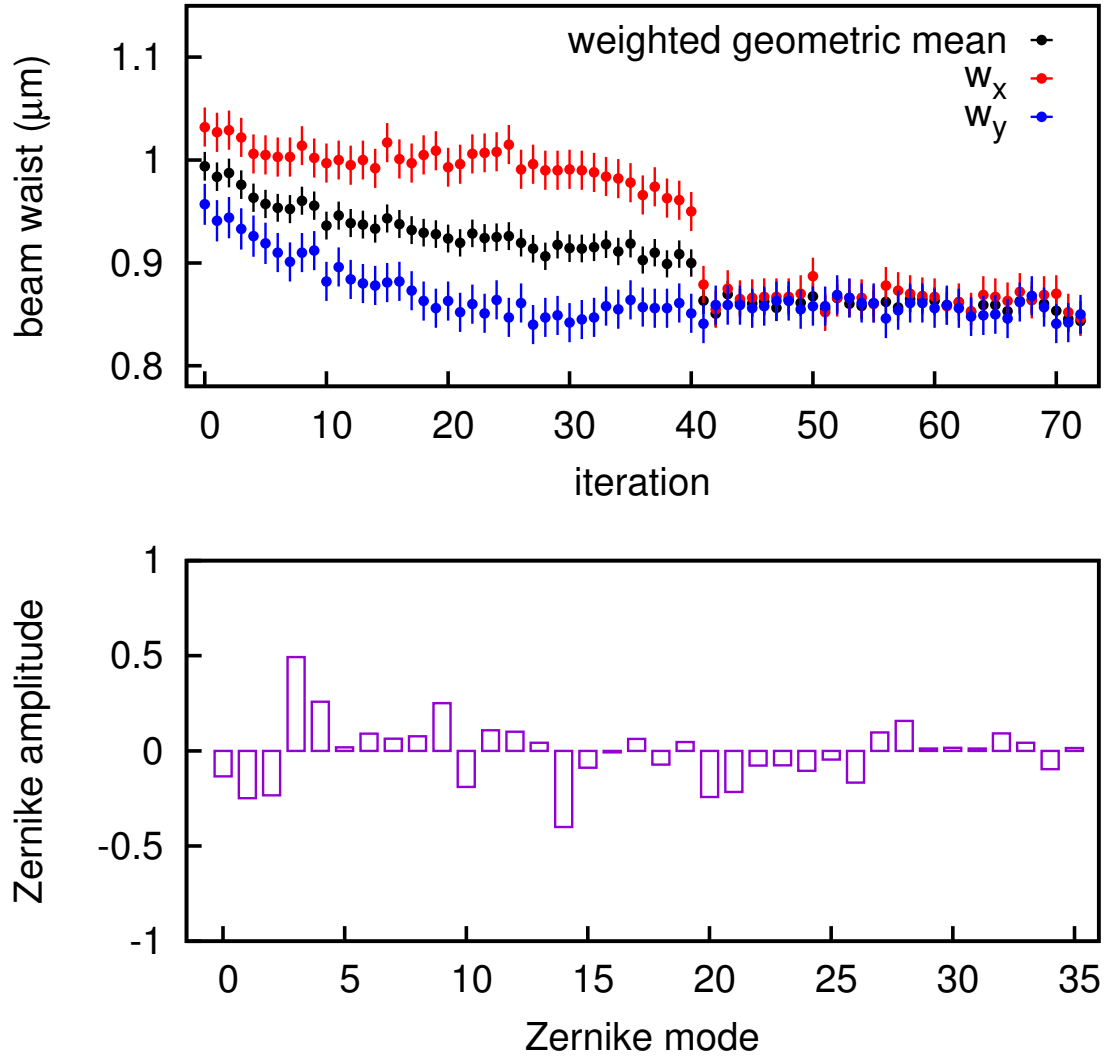


Figure 30: Top: optimized waist as a function of iteration steps. Red dots: waist data measured along x -axis. Blue dots: waist data measured along y -axis. Black dots: geometric mean of w_x and w_y weighted with relative power. Error bars represent one standard deviation of propagated fitting uncertainties. Bottom: Zernike decompositions of the phase mask.

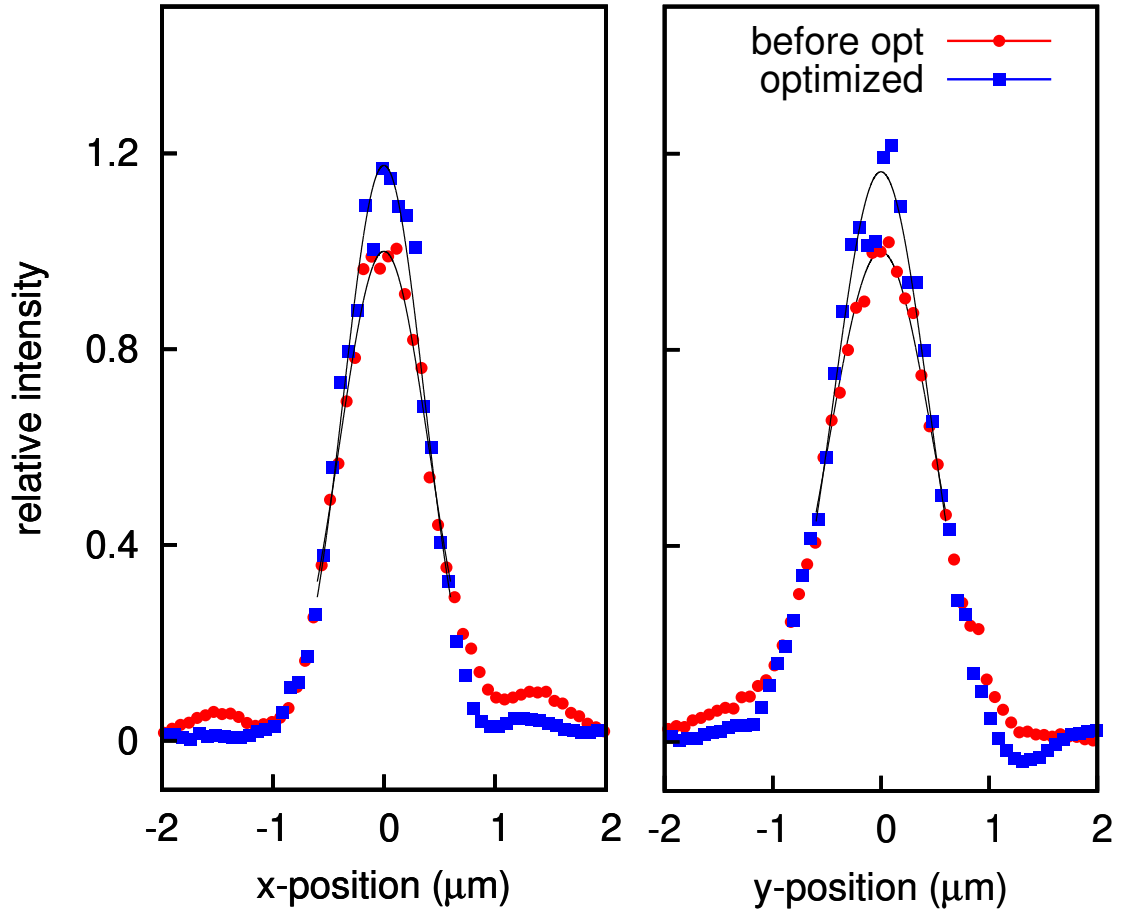


Figure 31: Intensity profile reconstructed from the discrete gradient of photodetector reading along the x - (left panel) and y -transverse axes (right panel) at the focus. The intensity is normalized with respect to the peak of beam profile before optimization. Red dots: light intensity before the area optimization. Blue dots: light intensity at the end of area optimization. Solid lines represent their respective Gaussian fit (Eqn 14), the best fit for the optimized beam radius shows $17.5 \pm 0.6\%$ (along x -axis) and $16.3 \pm 0.4\%$ (along y -axis) intensity improvement. Error bars (smaller than symbol size) represent one standard deviation of moving average.

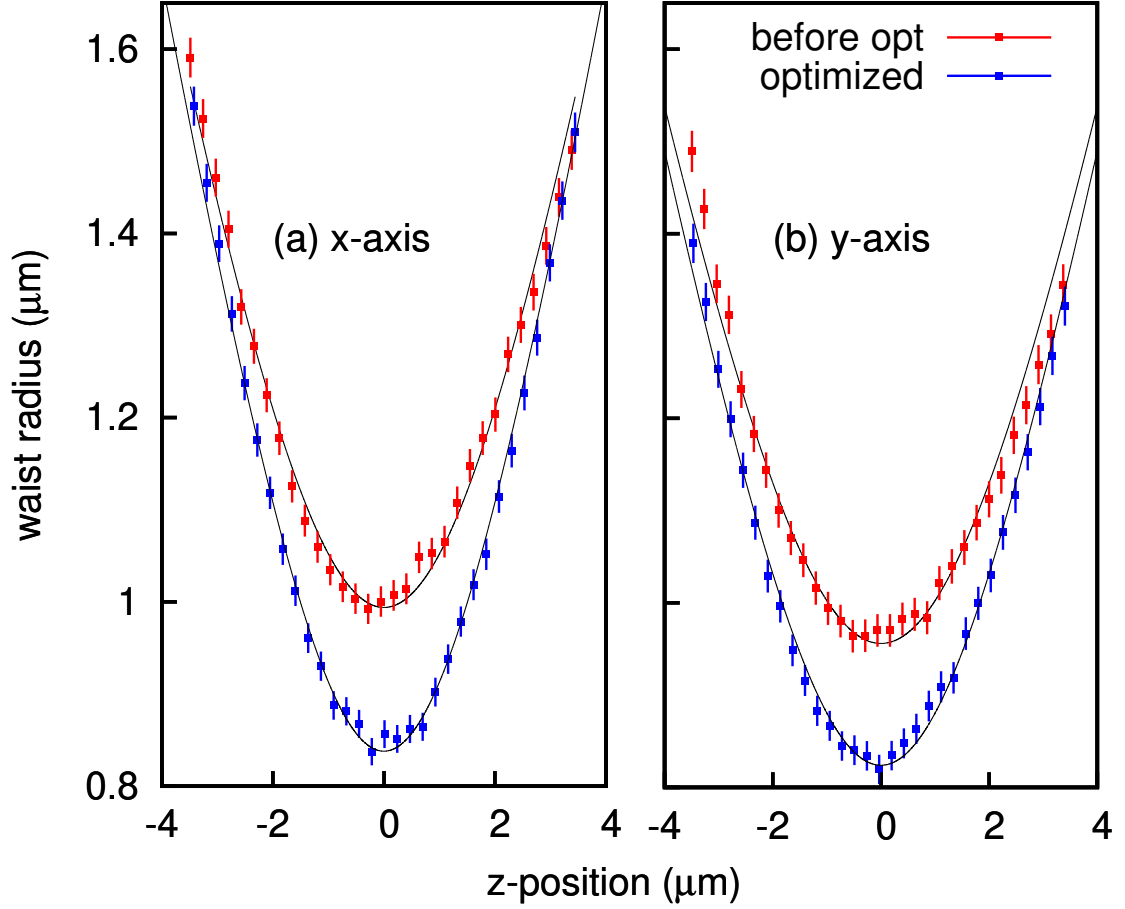


Figure 32: Beam radius in x - (left panel) and y -axes (right panel) as z is varied along the focus. Red dots: waist data before optimization. Blue dots: waist data after optimization. Black lines: best fit to the waists (Eq. 4) which gives the waist radius and M^2 . (a): Initial: $w_f = 994 \pm 4$ nm, $M^2 = 1.38 \pm 0.02$; optimized: $w_f = 838 \pm 2$ nm, $M^2 = 1.224 \pm 0.005$. (b): Initial: $w_f = 956 \pm 5$ nm, $M^2 = 1.16 \pm 0.04$; optimized: $w_f = 824 \pm 3$ nm, $M^2 = 1.03 \pm 0.01$. Error bars represent one standard deviation of propagated fitting uncertainties.

6 Conclusion and Ongoing Work

In this thesis, we investigated methods of improving the focusing properties of a high NA lens by pre-correcting optical aberrations in two dimensions via the introduction of a spatial light modulator (SLM). We used an automated beam profiling method based on the knife-edge method to analyze the transverse beam profile at the focus of the high NA lens. Several optimization schemes were proposed to generate the optimal phase pattern.

With an aspheric lens with numerical aperture (NA) of 0.55 and focal length of 4.51 mm, preliminary results of two one-dimensional optimizations show that focusing of laser beam can be improved using a SLM. The focal waist radius w_0 and beam quality factor M^2 before and after the optimization are measured and compared. For small focusing parameters, the optimized beam waist radii are smaller than the theoretical predictions for a collimated Gaussian beam at the expense of having larger beam quality factor M^2 . The reconstructed intensity profile shows a 30 % improvement in the peak intensity of the optimized beam for small focusing parameters. For larger focusing parameters, we still see a 14 % to 20 % improvement in the peak intensity.

Further investigation show that one-dimensional waist and intensity optimization algorithms do not always ensure the reduction in the focal spot size. We have developed an automated two-dimensional beam characterization method which can measure beam waist radii along two orthogonal axes. The new optimization scheme based on the weighted geometric mean of the beam radii demonstrates about 17.0 ± 0.4 % improvement in the peak intensity at the focus averaged over both axes.

From the observed improvement in intensity, aberration correction with the help of a SLM promises only a moderate improvement for atom-light efficiency.

One outcome of the work in this thesis is therefore that there is still one other physical reason for not obtaining the atom-photon coupling beyond the thermal motion of atom and the residual imaging aberrations. Nevertheless, it is of our interest to extend the scheme to optimize atom-light interaction efficiency in the setup with trapped atoms in the near future.

7 Appendices

7.1 SLM settings

7.1.1 Determination of Beam Position

We fashion the SLM as a knife-edge to determine the position of the center of the laser beam on the SLM screen (x_c, y_c) . Similar to how a physical knife-edge obstructs the transmission of light, we upload a region of random phase shift on the SLM to scatter part of the light incident on the SLM. By varying the area of the random phase shift region, the transmitted power of laser beam is fit to Eqn. 9 to determine the center position as well as the input beam radius.

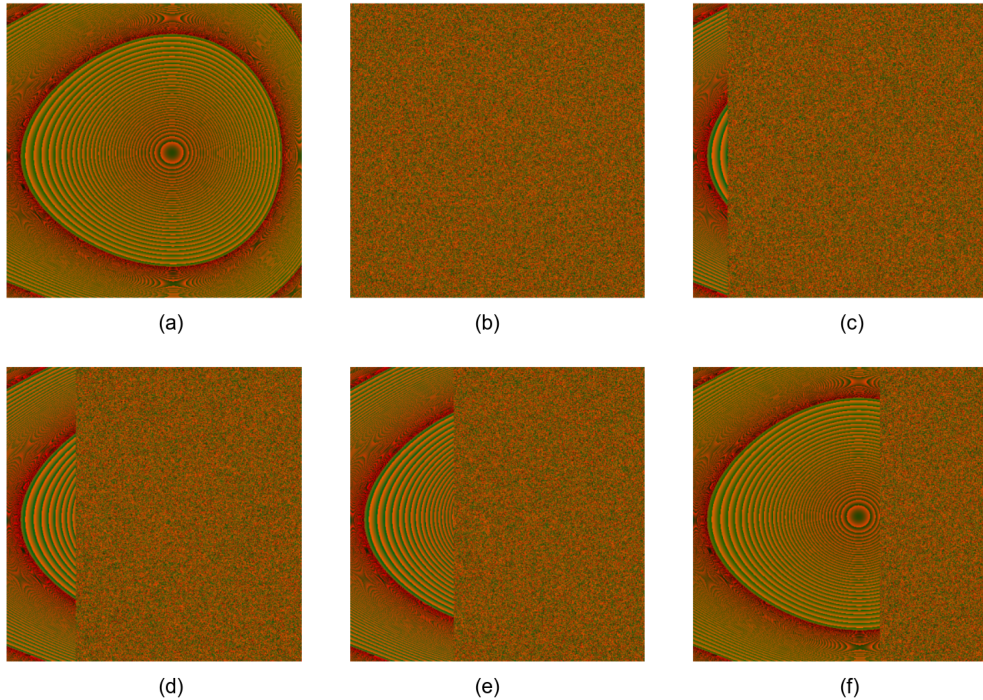


Figure 33: Phase masks uploaded to the SLM to determine center position. (a) fully reveals the beam and gives maximum transmitted power of laser beam. (b)-(f) varies the area of the random phase shift region to approximate a translating knife-edge.

7.1.2 Characteristic Radius

The phase mask generated based on Zernike polynomials takes the form of a disk. The radius of this disk on the SLM needs to meet with the effective aperture of the aspheric lens in order to correct its aberrations. To determine this characteristic radius, we compare the optimized weighted geometric mean of beam radii based on two-dimensional area optimization algorithm with different radii input on the SLM. We observe the best beam radii reduction when $r = 100$ pixels (which corresponds to 2.5 mm SLM radius for input beam radius w_{in} of 1.96 mm).

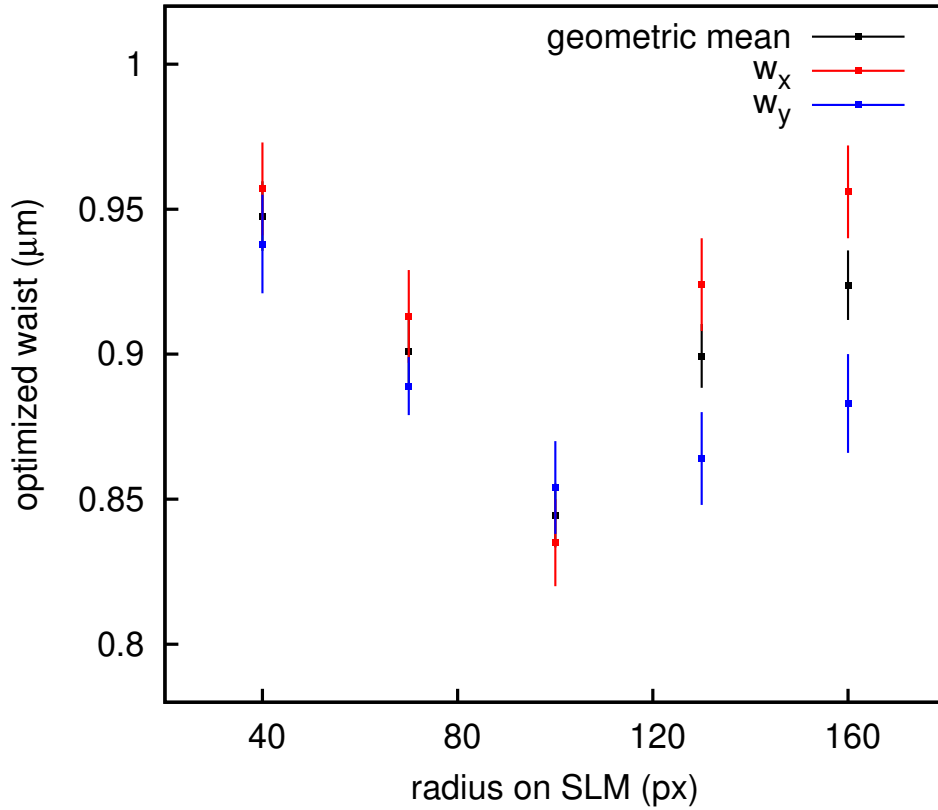


Figure 34: Optimization of the geometric mean of the beam radii at the focus with different sizes of phase mask. Red dots: waist data measured in x -axis. Blue dots: waist data measured in y -axis. Black dots: geometric mean of w_x and w_y weighted with relative power. Error bars represent one standard deviation of propagated fitting uncertainties.

7.2 Zernike Dimension

For each Zernike mode, the waist optimization algorithm typically takes 50 s of computational time. There is a trade-off between computational time and number of Zernike modes iterated over. Since higher orders of Zernike polynomials are less significant in beam radius optimization, we test the convergence of area optimization on $N = 10, 21, 36, 45$ and 91 (correspond to order 4, 6, 8, 9, 13 of Zernike polynomials) Zernike modes over two full cycles to determine the minimum number of Zernike modes required for convergence. We observe that the optimization algorithm reaches the convergence of $w \simeq 850$ nm for $N \geq 36$.

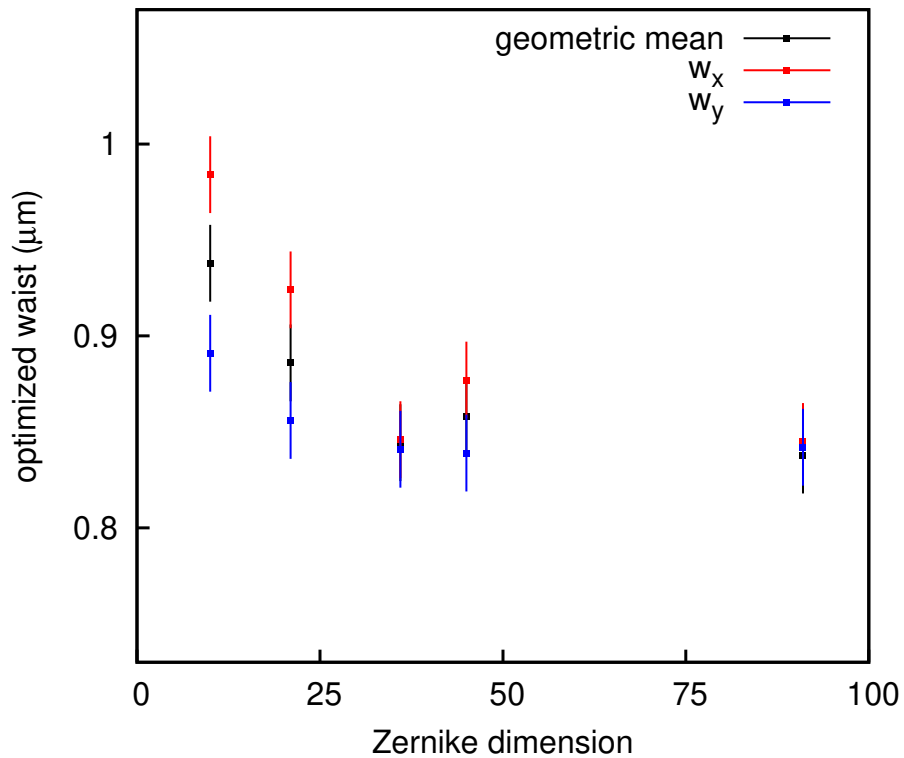


Figure 35: Optimization of the geometric mean of the beam radii at the focus with different number of Zernike modes. Red dots: waist data measured in x -axis. Blue dots: waist data measured in y -axis. Black dots: geometric mean of w_x and w_y weighted with relative power. Error bars represent one standard deviation of propagated fitting uncertainties.

References

- [1] N. Gisin and R. Thew, “Quantum communication,” *Nat Photon*, vol. 1, no. 3, pp. 165–171, 2007.
- [2] P. Kok, W. J. Munro, K. Nemoto, T. C. Ralph, J. P. Dowling, and G. J. Milburn, “Linear optical quantum computing with photonic qubits,” *Reviews of Modern Physics*, vol. 79, no. 1, pp. 135–174, 2007.
- [3] P. W. Shor, “Algorithms for quantum computation: discrete logarithms and factoring,” in *Proceedings 35th Annual Symposium on Foundations of Computer Science*, 1994, pp. 124–134.
- [4] L. K. Grover, “A fast quantum mechanical algorithm for database search,” *Proceedings of the twenty-eighth annual ACM symposium on Theory of computing - STOC '96*, pp. 212–219, 1996.
- [5] S. Boixo, S. V. Isakov, V. N. Smelyanskiy, R. Babbush, N. Ding, Z. Jiang, M. J. Bremner, J. M. Martinis, and H. Neven, “Characterizing quantum supremacy in near-term devices,” *Nature Physics*, vol. 14, no. 6, pp. 595–600, 2018.
- [6] H. J. Kimble, “The quantum internet,” *Nature*, vol. 453, no. 7198, pp. 1023–1030, 2008.
- [7] T. Wilk, A. Gaëtan, C. Evellin, J. Wolters, Y. Miroshnychenko, P. Grangier, and A. Browaeys, “Entanglement of Two Individual Neutral Atoms Using Rydberg Blockade,” *Physical Review Letters*, vol. 104, no. 1, p. 10502, jan 2010.

- [8] M. Saffman, T. G. Walker, and K. Mølmer, “Quantum information with Rydberg atoms,” *Reviews of Modern Physics*, vol. 82, no. 3, pp. 2313–2363, aug 2010.
- [9] L. M. Duan and C. Monroe, “Colloquium: Quantum networks with trapped ions,” *Reviews of Modern Physics*, vol. 82, no. 2, pp. 1209–1224, 2010.
- [10] I. Inlek, C. Crocker, M. Lichtman, K. Sosnova, and C. Monroe, “Multispecies Trapped-Ion Node for Quantum Networking,” *Physical Review Letters*, vol. 118, no. 25, p. 250502, jun 2017.
- [11] A. Reiserer, N. Kalb, M. S. Blok, K. J. van Bemmelen, T. H. Taminiau, R. Hanson, D. J. Twitchen, and M. Markham, “Robust Quantum-Network Memory Using Decoherence-Protected Subspaces of Nuclear Spins,” *Physical Review X*, vol. 6, no. 2, p. 21040, jun 2016.
- [12] A. Delteil, Z. Sun, W.-b. Gao, E. Togan, S. Faelt, and A. Imamolu, “Generation of heralded entanglement between distant hole spins,” *Nature Physics*, vol. 12, p. 218, dec 2015.
- [13] S. Ritter, C. Nölleke, C. Hahn, A. Reiserer, A. Neuzner, M. Uphoff, M. Mücke, E. Figueroa, J. Bochmann, and G. Rempe, “An elementary quantum network of single atoms in optical cavities,” *Nature*, vol. 484, p. 195, apr 2012.
- [14] A. Reiserer and G. Rempe, “Cavity-based quantum networks with single atoms and optical photons,” *Reviews of Modern Physics*, vol. 87, no. 4, pp. 1379–1418, dec 2015.
- [15] H. Takahashi, E. Kassa, C. Christoforou, and M. Keller, “Strong coupling of a single ion to an optical cavity,” pp. 1–10.

- [16] S. A. Aljunid, B. Chng, J. Lee, M. Paesold, G. Maslennikov, and C. Kurtsiefer, “Interaction of light with a single atom in the strong focusing regime,” *J. Mod. Opt.*, vol. 58, no. 3-4, pp. 299–305, 2011.
- [17] M. K. Tey, G. Maslennikov, T. C. Liew, S. A. Aljunid, F. Huber, B. Chng, Z. Chen, V. Scarani, and C. Kurtsiefer, “Interfacing light and single atoms with a lens,” *New J. Phys.*, vol. 11, 2009.
- [18] M. Sondermann, R. Maiwald, H. Konermann, N. Lindlein, U. Peschel, and G. Leuchs, “Design of a mode converter for efficient light-atom coupling in free space,” *Appl. Phys. B*, vol. 89, no. 4, pp. 489–492, 2007.
- [19] G. Zumofen, N. M. Mojarad, V. Sandoghdar, and M. Agio, “Perfect reflection of light by an oscillating dipole,” *Phys. Rev. Lett.*, vol. 101, no. 18, pp. 1–4, 2008.
- [20] D. J. Wineland, W. M. Itano, and J. C. Bergquist, “Absorption spectroscopy at the limit: detection of a single atom,” *Opt. Lett.*, vol. 12, no. 6, p. 389, 1987.
- [21] G. Wrigge, I. Gerhardt, J. Hwang, G. Zumofen, and V. Sandoghdar, “Efficient coupling of photons to a single molecule and the observation of its resonance fluorescence,” *Nat. Phys.*, vol. 4, no. 1, p. 60, 2008.
- [22] A. N. Vamivakas, M. Atatüre, J. Dreiser, S. T. Yilmaz, A. Badolato, A. K. Swan, B. B. Goldberg, A. Imamolu, and M. S. Ünlü, “Strong extinction of a far-field laser beam by a single quantum dot,” *Nano Lett.*, vol. 7, no. 9, pp. 2892–2896, 2007.
- [23] Y. S. Chin, M. Steiner, and C. Kurtsiefer, “Nonlinear photon-atom coupling with 4Pi microscopy,” *Nat. Commun.*, vol. 8, no. 1, pp. 1–13, 2017.

- [24] M. Fischer, M. Bader, R. Maiwald, A. Golla, M. Sondermann, and G. Leuchs, “Efficient saturation of an ion in free space,” *Appl. Phys. B Lasers Opt.*, vol. 117, no. 3, pp. 797–801, 2014.
- [25] L. Alber, M. Fischer, M. Bader, K. Mantel, M. Sondermann, and G. Leuchs, “Focusing characteristics of a 4 π parabolic mirror light-matter interface,” *J. Eur. Opt. Soc.*, vol. 13, no. 1, pp. 1–8, 2017.
- [26] L. Slodička, G. Hétet, S. Gerber, M. Hennrich, and R. Blatt, “Electromagnetically induced transparency from a single atom in free space,” *Physical Review Letters*, vol. 105, no. 15, pp. 1–4, 2010.
- [27] M. K. Tey, Z. Chen, S. A. Aljunid, B. Chng, F. Huber, G. Maslennikov, and C. Kurtsiefer, “Strong interaction between light and a single trapped atom without the need for a cavity,” *Nat. Phys.*, vol. 4, no. 12, pp. 924–927, 2008.
- [28] Y. S. Chin, M. Steiner, and C. Kurtsiefer, “Quantifying the role of thermal motion in free-space light-atom interaction,” *Phys. Rev. A*, vol. 95, no. 4, pp. 3–7, 2017.
- [29] F. L. Pedrotti and L. S. Pedrotti, *Introduction to Optics*. Prentice Hall, 1993.
- [30] A. E. Siegman, “Defining, measuring, and optimizing laser beam quality,” in *Laser Resonators and Coherent Optics: Modeling, Technology, and Applications*, vol. 1868. International Society for Optics and Photonics, 1993, pp. 2–13.
- [31] S. Quabis, R. Dorn, M. Eberler, O. Glöckl, and G. Leuchs, “Focusing light to a tighter spot,” *Opt. Commun.*, vol. 179, no. 1, pp. 1–7, 2000.

- [32] M. B. Schneider and W. W. Webb, “Measurement of submicron laser beam radii,” *Appl. Opt.*, vol. 20, no. 8, p. 1382, 1981.
- [33] R. L. McCally, “Measurement of Gaussian beam parameters,” *Appl. Opt.*, vol. 23, no. 14, p. 2227, 1984.
- [34] J. J. Chapman, B. G. Norton, E. W. Streed, and D. Kielpinski, “An automated submicron beam profiler for characterization of high numerical aperture optics,” *Rev. Sci. Instrum.*, vol. 79, no. 9, 2008.
- [35] I. Ilev, “Simple fiber-optic autocollimation method for determining the focal lengths of optical elements,” *Optics letters*, vol. 20, no. 6, pp. 527–529, 1995.
- [36] F. Zernike and J. E. Midwinter, *Applied nonlinear optics*. Courier Corporation, 2006.
- [37] A. D. Hill, D. Hervas, J. Nash, M. Graham, A. Burgers, U. Paudel, D. Steel, C. Schneider, M. Kamp, S. Höfling, J. Wang, J. Lin, W. Zhao, and P. G. Kwiat, “Optimizing single-mode collection from pointlike sources of single photons with adaptive optics,” *Opt. Express*, vol. 25, no. 16, p. 18629, 2017.
- [38] J. A. Carpenter and T. D. Wilkinson, “Aberration correction in Spatial Light Modulator based mode multiplexers,” *Opt. Fiber Commun. Conf. Fiber Opt. Eng. Conf. 2013*, no. c, p. JW2A.27, 2013.
- [39] A. Naber, H. J. Maas, K. Razavi, and U. C. Fischer, “Dynamic force distance control suited to various probes for scanning near-field optical microscopy,” *Review of Scientific Instruments*, vol. 70, no. 10, pp. 3955–3961, 1999.
- [40] X. Xie, L. Li, S. Wang, Z. Wang, and J. Zhou, “Three-dimensional measurement of a tightly focused laser beam,” *AIP Advances*, vol. 3, no. 2, 2013.

- [41] Y. Cai, Y. Liang, M. Lei, S. Yan, Z. Wang, X. Yu, M. Li, D. Dan, J. Qian, and B. Yao, “Three-dimensional characterization of tightly focused fields for various polarization incident beams,” *Review of Scientific Instruments*, vol. 88, no. 6, 2017.
- [42] C. J. Sheppard, N. K. Balla, and S. Rehman, “Performance parameters for highly-focused electromagnetic waves,” *Optics Communications*, vol. 282, no. 5, pp. 727–734, 2009.